

CARBON NANOTUBE SHEET SCROLLED FIBER COMPOSITE FOR ENHANCED
INTERFACIAL MECHANICAL PROPERTIES

by

PRUTHUL KOKKADA RAVINDRANATH

SAMIT ROY, COMMITTEE CHAIR

VINU UNNIKRISHNAN

MARK BARKEY

ANWARUL HAQUE

PAUL ALLISON

A DISSERTATION

Submitted in partial fulfillment of the requirements
for the degree of Doctor of Philosophy
in the Department of Aerospace Engineering and Mechanics
in the Graduate School of
The University of Alabama

TUSCALOOSA, ALABAMA

2017

ABSTRACT

The high tensile strength of Polymer Matrix Composites (PMC) is derived from the high tensile strength of the embedded carbon fibers. However, their compressive strength is significantly lower than their tensile strength, as they tend to fail through micro-buckling, under compressive loading. Fiber misalignment and the presence of voids created during the manufacturing processes, add to the further reduction in the compressive strength of the composites. Hence, there is more scope for improvement.

Since, the matrix is primarily responsible for the shear load transfer and dictating the critical buckling load of the fibers by constraining the fibers from buckling, to improve the interfacial mechanical properties of the composite, it is important to modify the polymer matrix, fibers and/or the interface.

In this dissertation, a novel approach to enhance the polymer matrix-fiber interface region has been discussed. This approach involves spiral wrapping carbon nanotube (CNT) sheet around individual carbon fiber or fiber tow, at room temperature at a prescribed wrapping angle (bias angle), and then embed the scrolled fiber in a resin matrix. The polymer infiltrates into the nanopores of the multilayer CNT sheet to form CNT/polymer nanocomposite surrounding fiber, and due to the mechanical interlocking, provides reinforcement to the interface region between fiber and polymer matrix. This method of nano-fabrication has the potential to improve the mechanical properties of the fiber-matrix interphase, without degrading the fiber properties.

The effect of introducing Multi-Walled Carbon Nanotubes (MWNT) in the polymer matrix was studied by analyzing the atomistic model of the epoxy (EPON-862) and the embedded

MWNTs. A multi-scale method was utilized by using molecular dynamics (MD) simulations on the nanoscale model of the epoxy with and without the MWNTs to calculate compressive strength of the composite and predict the enhancement in the composite material. The influence of the bias/over wrapping angle of the MWNT sheets on the carbon fiber was also studied.

The predicted compressive strength from the MD results and the multiscale approach for baseline Epoxy case was shown to be in good relation with the experimental results for Epon-862. On adding MWNTs to the epoxy system, a significant improvement in the compressive strength of the PMC was observed. Further, the effect of bias angle of MWNT wrapped over carbon fiber was compared for 0° , 45° and 90° . This is further verified by making use of the Halpin-Tsai.

DEDICATION

This dissertation is dedicated to my parents and my brother, who are always a positive influence in my life, my friends who constantly motivated and cheered me to achieve this milestone. I am really thankful for their support and help through this journey, and making it one of the most valuable experiences of my life.

LIST OF ABBREVIATIONS AND SYMBOLS

PMC	Polymer Matrix Composites
CNT	Carbon nanotube
MWNT	Multi-walled carbon nanotube
MD	Molecular Dynamics
wt%	Weight percent
CFRP	Carbon fiber reinforced polymer composites
SWNT	Single-walled carbon nanotube
CVD	Chemical Vapor Deposition
RVE	Representative Volume Element
DETDA	Diethyltoluenediamine
IFSS	interfacial shear strength
OPLS	Optimized Potentials for Liquid Simulations
ReaxFF	Reactive Force Field
LAMMPS	Large-scale Atomic/Molecular Massively Parallel Simulator
SEM	Scanning electron microscopy
ϕ_0	Fiber Misalignment Angle
α	Overwrap or Bias Angle

ACKNOWLEDGMENTS

I am pleased to have this opportunity to thank all my colleagues and faculty members who have helped me with this research project. I am indebted to Dr. Samit Roy, my academic advisor, for being a constant source of guidance and help throughout the course of this project. I would like to thank Dr. Unnikrishnan for his valuable input on nanoscale simulations, Dr. Barkey for his help with experimental analysis and for always being there when I needed his guidance. I would also like to thank my committee members, Dr. Anwarul Haque and Dr. Paul Allison for their support and guidance during both my dissertation and academic progress. I would also like thank Dr. Hongbing Lu, Dr. Ray Baughman and their research group from University of Texas at Dallas for their collaboration in this project and sharing with us all the data and information from their experimental research.

This research would not have been possible without the support of my fellow graduate students, Avinash Akepati, Abhishek Kumar, Shibo Li, Daigo Seki, Ankit Srivastav and Anubhav Roy for always lending a helping hand and their motivation throughout this research and to AFOSR, for funding the project. I am thankful and forever indebted to Dr. Gregory Odegard for introducing me to the world of Molecular Dynamics. I would also like to thank Dr. Ben Jensen and Dr. Ananyo Bandyopadhyay for teaching me and helping me with nanoscale simulations.

Finally I thank my family and friends for always believing in me and constantly motivating me with their moral and emotional support and for bringing out the best in me.

CONTENTS

ABSTRACT.....	ii
DEDICATION.....	iv
LIST OF ABBREVIATIONS AND SYMBOLS	v
ACKNOWLEDGMENTS	vi
LIST OF TABLES	x
LIST OF FIGURES	xi
CHAPTER 1 INTRODUCTION	1
CHAPTER 2 LITERATURE REVIEW	8
2.1 MATERIALS USED.....	8
2.1.1 Fiber Reinforced Polymer Composites.....	8
2.1.2 Epoxy Resins	10
2.1.3 Carbon Nanotubes	13
2.2 CARBON NANOTUBE REINFORCED FIBER COMPOSITES	15
2.2.1 Background:.....	15
2.2.2 Carbon Nanotube Sheet Scrolled Carbon Fiber In Polymer Composites.....	18
2.3 MULTISCALE MODELING	21
2.4 MOLECULAR DYNAMICS SIMULATIONS	23

2.4.1 Introduction	23
2.4.2 Algorithms	24
I. VERLET ALGORITHM.....	24
II. LEAP-FROG ALGORITHM.....	25
III. BEEMAN’S ALGORITHM.....	26
IV. VELOCITY VERLET ALGORITHM.....	26
2.4.3 Ensembles, Thermostats and Barostats	27
2.4.4 Boundary Conditions:.....	31
2.5 FORCE FIELD POTENTIALS	33
2.5.1 Introduction	33
2.5.2 OPLS	36
2.5.3 ReaxFF.....	40
2.6 SIMULATION PROCEDURE	43
2.7 LAMMPS OVERVIEW	45
2.8 OVITO	46
CHAPTER 3 MULTISCALE MODELING METHODOLOGY FOR PREDICTING COMPRESSIVE STRENGTH ENHANCEMENT IN CARBON FIBER REINFORCED COMPOSITES USING SCROLLED MWNT SHEET	47
3.1 MULTISCALE APPROACH	47
3.1.1 Introduction:	47
3.1.2 Macromechanics:.....	48

3.1.3 Micromechanics:	50
3.1.4 Nanoscale Simulations:	51
3.1.5 Influence of Strain Rate:.....	54
3.2 COMPUTATIONAL MODELING DETAILS	56
CHAPTER 4 RESULTS AND DISCUSSION.....	64
4.1 Baseline Epoxy Model (Case I) With Interpolation For Strain Rate Effect.....	65
4.2 Modeling Epoxy Embedded with One and Four MWNTs (Case II and IV) With Interpolation For Strain Rate Effect	69
4.3 Study of the influence of Overwrap Angle of MWNT sheet on carbon fiber With Interpolation For Strain Rate Effect	73
4.4 Experimental Verification	81
CHAPTER 5 CONCLUSIONS AND FUTURE WORK.....	89
5.1 Conclusions:	89
5.2 Future Work	92
REFERENCES	93

LIST OF TABLES

3.1 Case studies with interpolation for strain rate effect.....	60
4.1 Compressive strength of baseline CFRP from MD simulations at different strain rates.....	68
4.2 Compressive strength enhancement comparison on adding one and four MWNTs, from MD simulations, at the reference strain rate of 0.01 /sec for shear deformation applied perpendicular to the MWNT axis at a strain rate of 0.01.....	72
4.3 Compressive strength enhancement comparison on adding one MWNT at 0°, 45° and 90° bias angle, at the reference strain rate of 0.01/sec.....	75
4.4 Compressive strength enhancement comparison on adding four MWNT at 0°, and 90° shear deformation angles, at the reference strain rate of 0.01/sec at 300 K.....	77
4.5 EPON-862 and MWNT properties for Halpin-Tsai calculation.....	80
4.6 Comparison of Halpin-Tsai calculations with MD simulation results for a strain rate of 0.01/sec.....	80
4.7 Modulus from nanoindentation tests.....	82
4.8 Modulus of the interface region between epoxy-MWNT from MD simulations and multiscale approach computed at a strain rate of 0.001/sec.....	83
5.1 Compressive strength comparison for cases I-VI, at the reference strain rate of 0.01/sec.....	91

LIST OF FIGURES

1.1 Compact tension fracture test results for baseline and nanographene reinforced EPON 862 epoxy specimens.....	2
1.2 A schematic diagram showing a MWNT scrolling a carbon fiber and SEM images.....	5
1.3 Schematic diagram showing a multiscale approach to calculate the improvement in the Compressive Strength in MWNT scrolled Fiber/Epoxy Composite.....	7
2.1 Tensile and Compressive Strength of Unidirectional Carbon Fiber Composites.....	9
2.2 Epoxide ring with two reacting Carbon and one Oxygen atoms and DETDA.....	10
2.3 Formation of EPON 862.....	12
2.4 Schematic of Carbon nanotubes showing folded layer of graphene.....	13
2.5 TEM images of MWNT.....	17
2.6 MWNT forest conversion into sheets and assembly into sheets.....	18
2.7 Load vs Displacement for pull-out and push-in tests.....	19
2.8 Length scales involved in the multiscale modeling.....	22
2.9 Schematic of a system with periodic boundary.....	32
2.10 Schematic of dihedral angle.....	38
2.11 Variation in L-J potential with inter-particle distance.....	40
2.12 Schematic of bond order relation with interatomic distance.....	42
2.13 Algorithm of a generalized Molecular Dynamics Simulation.....	44
3.1 A schematic diagram showing a multiscale approach to calculate the improvement in the Compressive Strength in MWNT scrolled Fiber/Epoxy Composite.....	48
3.2 Representative Volume Element Loaded in Shear.....	51
3.3 MD model of MWNT/Epon-862/Carbon Fiber Interface and Virial shear stress vs. strain curve indicating shear modulus and plastic strain at yield.....	52

3.4 Molecular Model of Epoxy-MWNT interface.....	52
3.5 Case I – RVE showing MD model of Baseline Epoxy, EON 862, under uniform shear deformation.....	57
3.6 Schematic of MWNT sheet scrolled on carbon fiber at a bias angle of α	59
3.7 RVE showing four MWNT/Epoxy Interface shear deformation for Case II, III, IV, V.....	62
3.8 RVE showing four MWNT/Epoxy Interface shear deformation for Case VI.....	63
4.1 Shear Stress vs Strain at different strain rates for EPON-862 at 300K.....	65
4.2 Log Shear Stress vs Log Strain for EPON-862 at 300 K under different strain rates.....	66
4.3 Variation of the power law intercept A and exponent n for EPON-862 matrix at 300 K for with their corresponding normalized strain rates.....	67
4.4 Shear Stress vs Strain comparison for Case II RVE - Epoxy with four MWNT, at different strain rates at 300K.....	70
4.5 Shear Stress vs Strain comparison for Case IV RVE - Epoxy with one MWNT, at different strain rates at 300K.....	70
4.6 Shear Stress vs Strain comparison between Baseline Epoxy, Epoxy with one MWNT and Epoxy with Four MWNT at a strain rate of 2.43×10^{11} /sec at 300K.....	71
4.7 Shear Stress vs Strain comparison between Baseline Epoxy, Epoxy with One MWNT under shear deformations at angles 0° , 45° and 90° at a strain rate of 2.43×10^{11} /sec.....	74
4.8 Shear Stress vs Strain comparison between Baseline Epoxy, Epoxy with Four MWNT under shear deformations at angles 0° and 90° at a strain rate of 2.43×10^{11} /sec at 300K.....	76
4.9 Modulus estimation from nanoindentation tests.....	81
4.10 Compressive Stress vs Strain for epoxy with one and four MWNTs at a strain rate of $1 \times 10^{10} \text{ sec}^{-1}$ at 300 K.....	83
4.11 Schematic of MWNT sheet scrolled single carbon fiber RVE.....	84
4.12 3-Point Bending schematic.....	86

CHAPTER 1

INTRODUCTION

Composite materials offer many advantages over traditional material systems such as higher specific strength and stiffness, high thermal and electrical conductivity, low weight, easier installation, fabrication tailorability, and improved safety among others. These advantages have led to widespread usage of composites by replacing conventional materials in the aerospace, automobile and biomedical industries. The low weight of the composite structures with the high strength properties, have helped significantly in cutting down the fuel costs and CO₂ emissions. Many aerospace companies have incorporated more than 50% of polymer based composites in their new line of products in the recent years [1, 2] and have steadily decreased the use of metals. Other than aerospace industry, polymer based composites (PMCs) are extensively used in the automobile and biomedical industries. Prosthetics made out of composites are preferred because of their flexibility in fabrication, low weight, high tensile strength and low maintenance compared to their metal counterparts. The low weight-high strength properties are also extensively made use of by the automobile industry in high performance vehicles for engines, transmissions, exterior and interiors.

Higher initial costs pose a major obstacle towards more widespread application of composites. Extensive research is being conducted to reduce the manufacturing costs of composites and to improve their mechanical properties. Significant improvements in the mechanical properties of polymer based composites were observed by introducing few weight percentages of nanoparticles into the polymers [3-7]. Compact-tension (CT) fracture tests conducted by Roy et al., [4] (as shown in Figure 1.1), observed that the peak failure load

increased by 141% and 190% and a corresponding fracture toughness by 142% and 200% over the baseline epoxy at room temperature, when just 0.1wt% and 0.5 wt% of nanographene additives respectively, were introduced to the epoxy. Similar enhancements in fracture properties of graphene reinforced epoxy were reported by other researchers [8]. The enhancement in the properties of a material observed at the macroscale can be attributed to the nanoscale interactions between the constituent materials.

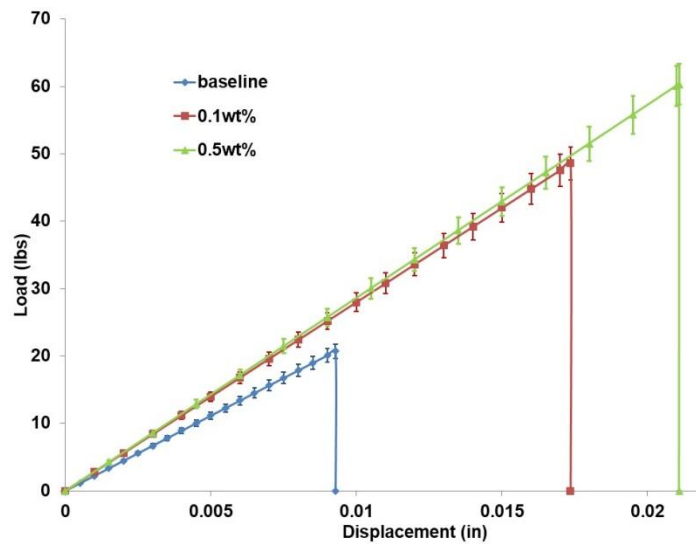


Figure 1.1 Compact Tension Fracture Test Results for Baseline and Nanographene Reinforced EPON-862 Epoxy Specimens (at Room Temperature) [4]

The high strength of carbon fibers contributes to the high tensile strength of Carbon Fiber Reinforced Polymer Composites (CFRP). Fibers typically have high tensile strength; however, their compressive strength is generally much lower at about 50% of their tensile strength. This is primarily because; fibers tend to fail through micro-buckling (or kinking) under compressive loading, before compressive fracture. The presence of voids and fiber misalignment during the manufacturing process further contributes to the reduction in compressive strength. The mechanical load transfer in carbon fiber reinforced polymer (CFRP) composites is often limited

by the strength of the interface region between fiber and the matrix. This leaves room for the improvement of compressive strength of CFRP [9]. In a composite system, load transfer takes place through the interface between the fiber and polymer matrix, and the interfacial region is primarily responsible for shear load transfer and governs the critical buckling load of the fibers by constraining the fibers [10]. The stiffness and transfer strength of fiber reinforced composite depends primarily on the thickness of the interface region on the order of 100 nm or less.

Swadner et al. [11] determined that the failure or delamination of a glass fiber occurs in the matrix at about 3 nm away from the fiber surface. Similar behavior was also observed for Single Walled Carbon Nanotubes (SWNT) nanocomposites. It was also observed by Ding et al [12] that a small amount of polycarbonate remains wrapped around a SWNT when it is pulled out of the polycarbonate matrix during fracture. Therefore, to increase the matrix-dominated properties of composites, such as interfacial shear and compressive strength, it is very important to improve the interfacial mechanical properties by modifying the polymer matrix and/or the interface.

In recent years, a lot of effort has been directed towards strengthening the matrix by adding nanofillers to the matrix to make nanocomposites [13, 14]. Carbon Nanotubes (CNTs) offers strength of 100 GPa and modulus of 1 TPa along with high thermal conductivity and electrical properties [15]. These superior properties of the CNTs can be utilized to enhance the corresponding interfacial properties for CFRPs. A common method to increase the interfacial stiffness and strength is by grafting CNTs on carbon fibers using Chemical Vapor Deposition (CVD) method which requires higher operational temperatures, sometimes referred to as “fuzzy fibers technique” [16-27]. However, this often leads to degradation of in-plane fiber properties due to these high processing temperatures. As a focus of this dissertation, a unique mechanism

was studied, to avoid the thermal degradation of the carbon fibers and achieve the nanotube reinforcement at room temperatures.

OBJECTIVE:

As the part of an AFOSR funded project, a different approach was used to resolve this issue. It is proposed, to spiral wrap CNT sheets around an individual carbon fiber or a carbon fiber tow. Figure 1.2 describes a schematic of scrolling MWNT sheets on carbon fibers. The CNT sheet drawn from either SWNT or MWNT forest is meso-porous with high specific surface area, because of which even small amount of CNT sheet in weight, can be used to wrap around large volume of carbon fibers. This CNT sheet overwrapped carbon fiber is subsequently embedded in a polymer matrix, which infiltrates the nanopores of the multilayer CNT sheet to form mechanically-interlocked CNT/polymer nanocomposite surrounding the fiber. The high-volume fraction of the CNT in the matrix provides the reinforcement to the interface region of polymer and fiber due to mechanical interlocking. This approach directly influences the compressive strength of the composite without degrading fiber properties. While the CNT/polymer nanocomposite surrounding a fiber is anticipated to provide enhanced thermal and electrical conductivities to the overall composite, the principal goal of this dissertation is to investigate the effects of CNT sheet scrolled fibers on the interfacial mechanical properties, with the targeted focus on improving primarily the interfacial shear and compressive strengths.

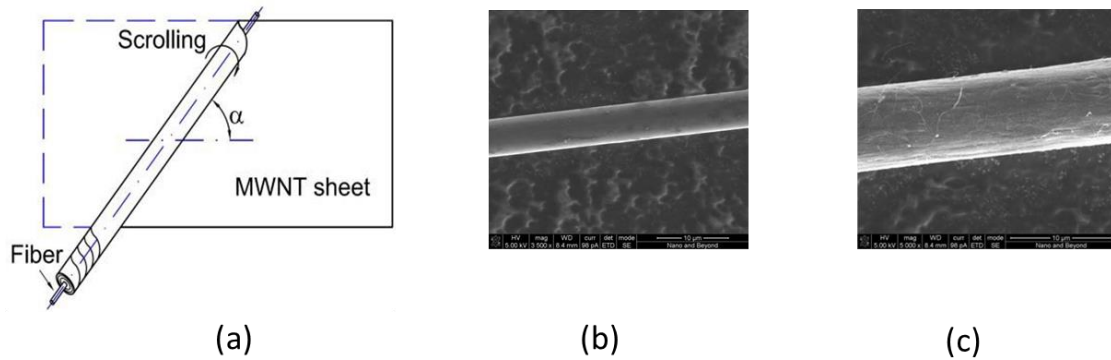


Figure 1.2: (a) A Schematic Diagram Showing a MWNT Scrolling a Carbon Fiber; (b & c) Different Segments of the Same Carbon Fiber With and Without Scrolled MWNT Sheet. The Same Magnification was used in both SEM Micrographs. (b) A Segment of the Single Carbon Fiber. (c) A Segment of the Same Single Carbon Fiber With MWNT Plies Scrolled Around it. The Scrolled MWNT Sheet has increased the Diameter by nearly 150%

For a typical nanoparticle reinforced carbon fiber polymer-matrix composite, the strength of the polymer matrix is enhanced by the nanoscale interaction with the nanoparticle reinforcement. The carbon fiber diameter that could range from 5-10 microns and the length that could range up to several meters, in combination with the reinforced CNT sheets, embedded in the polymer matrix, results in orthotropic properties in the macroscale. Hence, the nanoscale interaction between the polymer molecules and the nanoparticles is a key factor in determining the macroscale enhancement of the composite. Therefore, to characterize and better understand the local influence of the nanoparticle on the mechanical properties of the composite, it is important to understand the nanoscale and microscale behavior of its constituents. This is achieved by performing multi-scale simulations. Because of the computational limitations, preparing a comprehensive model of a macroscale aerospace structure with its nanoscale details is currently impractical, and hence a multi-scale model is needed to bridge the gap between the length and time scales. A hierarchical nano-micro-macroscale model was developed to identify the

mechanisms that govern the compressive strength enhancement in a composite, and this model was validated using available experimental test data.

While the use of hierarchical multiscale modeling in composites is not novel, the application of hierarchical multiscale models to predict the compressive strength of a nanoparticle reinforced unidirectional carbon/epoxy composite has not been attempted to date. To perform a nanoscale analysis of this system, Molecular Dynamics (MD) technique of computational simulations was used, which uses Newtonian laws of motion in a group of particles/atoms, to give information on system dynamics in the atomic scale. Thermal motions of the atoms are implemented through the use of a thermostat. An atomistic model of the interface region between the polymer matrix and the MWNT was prepared and the shear deformation was applied on this nanoscale RVE using MD simulations. The nanoscale virial stresses in the composite RVE obtained from MD simulations were used to calculate the composite shear modulus at 50% fiber volume fraction using the rule of mixtures, with and without the MWNTs. In this manner, the effect of carbon fiber volume fraction and orthotropy of the micromechanical composite RVE at the next higher length scale was incorporated in the model. Subsequently, the composite shear moduli of two cases (with and without MWNTs), were incorporated in modified Argon's formula to calculate the macroscale compressive strength [28]. The influence of carbon fiber misalignment at the macro-scale was incorporated in the multi-scale model in this manner. A schematic of the hierarchical multiscale modeling approach is shown in Figure 1.3, which briefly explains our approach of using the nanoscale information provided by the MD simulation on the interface region between epoxy and MWNTs, into a microscale formula the results from which is then used to calculate the macroscale value of compressive strength.

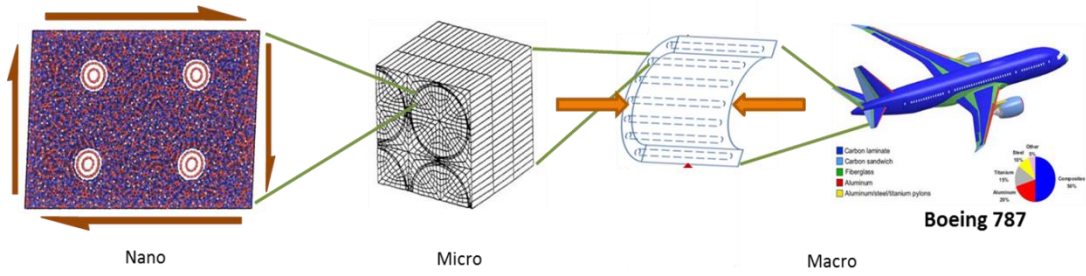


Figure 1.3: Schematic Diagram Showing a Multiscale Approach to Calculate the Improvement in the Compressive Strength in MWNT Scrolled Fiber/Epoxy Composite

CHAPTER 2

LITERATURE REVIEW

2.1 MATERIALS USED

2.1.1 Fiber Reinforced Polymer Composites

Fiber reinforced polymer matrix composites have found increasing applications in industries like aerospace, automotive, wind farms, offshore drilling, sports and construction. The combination of fibers embedded in a polymer matrix creates materials with properties exceeding that of the individual components. Carbon fiber reinforced polymer (CFRP) composites comprise of strong and stiff carbon fibers and load transferring polymer matrix material. The improved mechanical performance, like excellent specific stiffness and strength, low weights are driving factors for increased use as advanced composite materials in structural applications. Along with the high specific stiffness, their high resistance to fatigue and corrosion, which in turn significantly lowers the maintenance costs, makes them highly desirable material in the engineering fields and products. The usage of CFRPs as advanced composites in aircrafts has rapidly increased since their commercial availability [1, 2]. Boeing 787 is a good example of one of the recent commercial aircrafts that have incorporated CFRPs and other composite materials to about 50% of the material weight [1].

CFRP composites' substantial heterogeneity and anisotropy provides for their complex failure mechanism which are difficult to predict. They are affected by many failure modes that may initiate and interact to result in the ultimate failure of the component. Material behavior like size effects, moisture, temperature, presence of voids, fiber misalignments during the fabrication, may further contribute to their failure. In the case of compressive strength, specifically, under

compression loading, failure is often caused by delamination, microbuckling or kinking [28]. It is shown that for unidirectional CFRP the compressive strength is relatively lower than the tensile strength. Figure 2.1 shows the comparison between the tensile and compressive strength of different grades of carbon fiber in unidirectional lamina [29]. From this figure it can be seen that the compressive strength is about 20 to 60% of their tensile strength. This limits the use of the CFRPs in structural applications that undergo compressive loading.

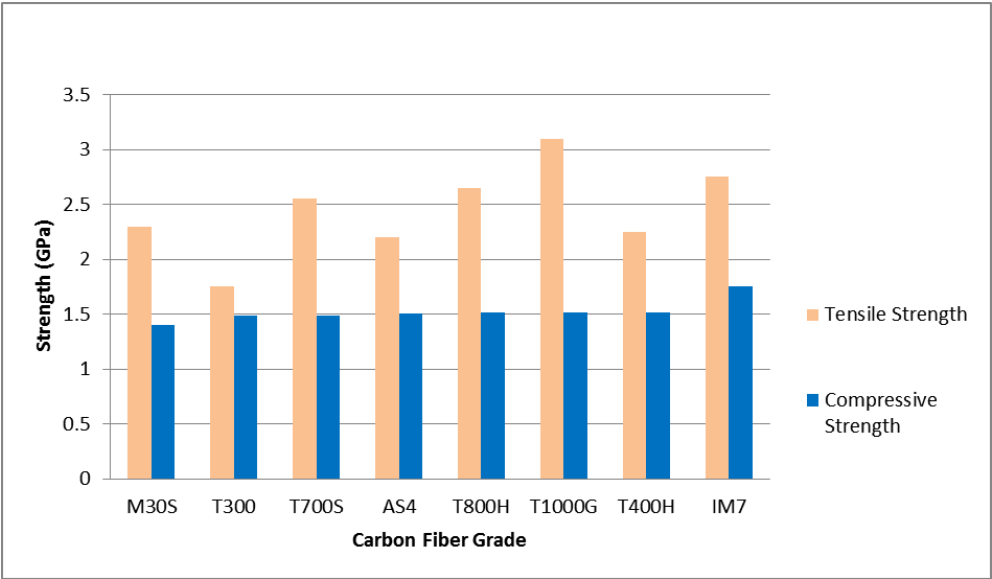


Figure 2.1: Tensile and Compressive Strength of Unidirectional Carbon Fiber Composites [29]

Hence, there is much room for improvement to increase the compressive strength of CFRP and extensive research is necessary to realize the enhancement in the compressive strength.

2.1.2 Epoxy Resins

Polymer composites have excellent specific stiffness, specific strength and processing properties, which makes them highly desirable in the modern aerospace and automobile industries. The molecular scale structure of the epoxy composites influences their mechanical properties and hence to achieve design optimization a good understanding of the structure-property relationship is required.

Epoxy resins comprises of epoxide group, also known as oxiran or ethoxyline group, which is a three membered oxide ring as shown in Figure 2.2 (a) [30]. The resin compounds containing more than one epoxide group per monomer polymerize at the epoxy groups with the hardener or curing agent. The polymerization process that the monomer undergoes with the hardener, forms a three dimensional network which is tougher and denser than its original constituents [30].

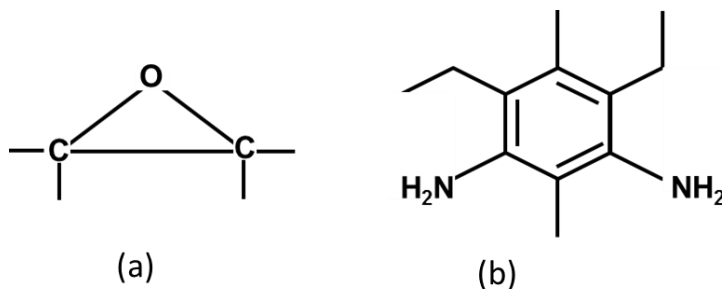


Figure 2.2: (a) Epoxide Ring with Two Reacting Carbon and One Oxygen Atoms (b) DETDA (diethyltoluenediamine)

For the purpose of this dissertation, the cured EPON 862 epoxy with DETDA (diethyltoluenediamine) or curing agent W (Figure 2.2 (b)) [31], is taken into consideration. The detailed curing process of EPON 862 polymer is discussed as follows [32, 33]. An epoxide with

an 'R' group, typically is chlorine based, is combined with Bisphenol F to form EPON 862 (Figure 2.3 (a)). A side reaction to this newly formed EPON 862 is the reaction of EPON 862 with excess Bisphenol F to form long chained modified EPON 862 with an epoxide group on each end (Figure 2.3 (b)). But, since this reaction is heat dependent, it can be controlled. Next, the EPON 862 monomer is cured with the DETDA. Based on molecular mixture calculations, a cure ratio of 2:1 is used, where, two molecules of resin combines with one molecule of the curing agent. Here the hydrogen atom of the amine groups of DETDA reacts with the epoxide group of EPON 862 (Figure 2.3 (c)). Since three more hydrogen atoms are present in the two amine groups, the resulting molecule can react with up to three more epoxide groups, starting a cross-linking chain between the EPON 862 molecule and the DETDA hardener (Figure 2.3 (d)). This process then can continue to react with the epoxide and the amine groups, making a strong crosslinked three dimensional network.

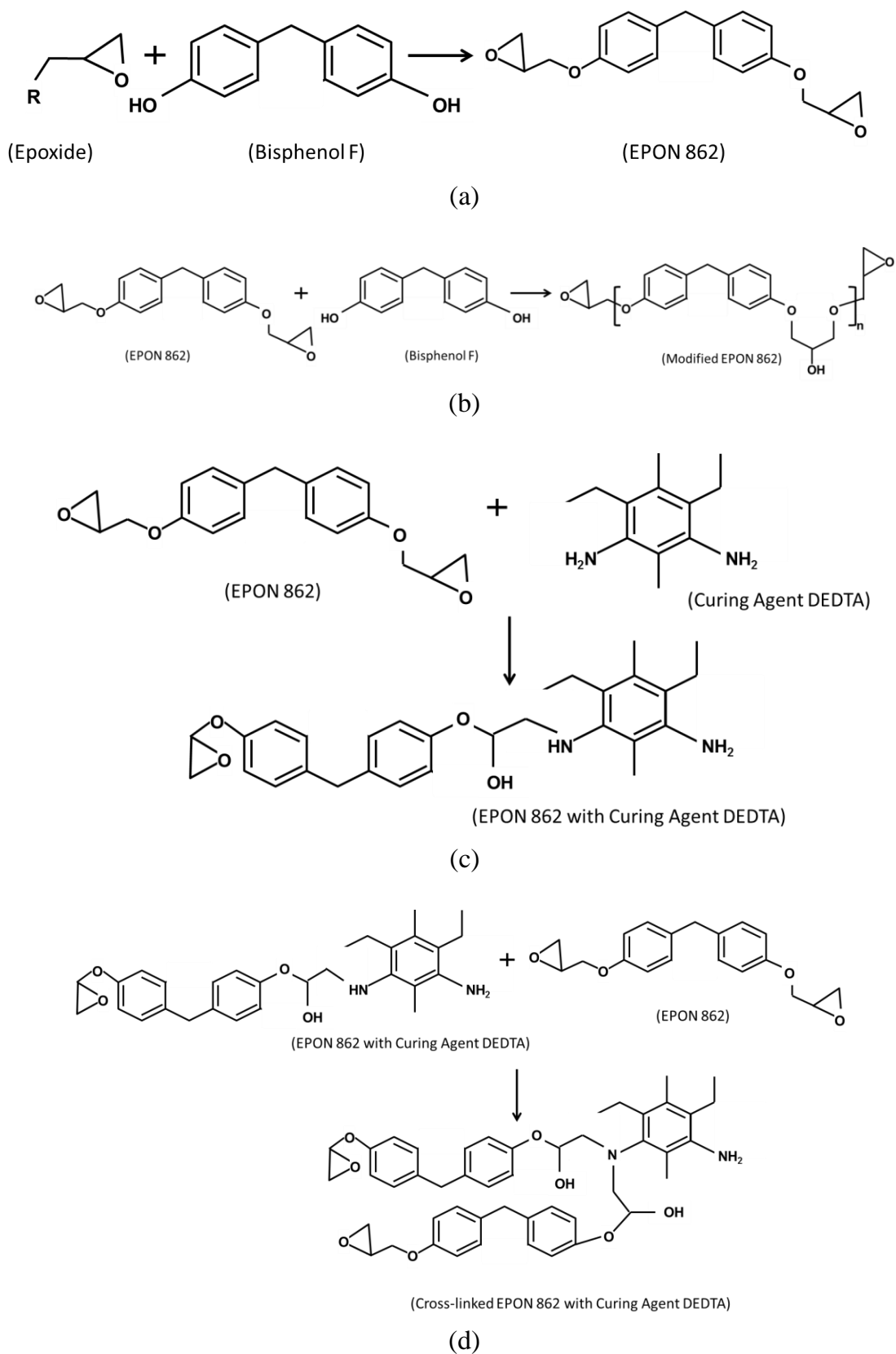


Figure 2.3: (a) Formation of EPON 862, (b) Adding of Bisphenol F to EPON 862, (c) Reaction of EPON 862 with Curing Agent DETDA, (d) Start of Cross-linking of EPON 862 and Curing Agent

2.1.3 Carbon Nanotubes

Carbon Nanotubes (CNTs) are hollow graphene cylindrical elongated fullerenes with diameter ranging from sub-nanometers to tens of nanometers and closed at their either end with pentagonal ring caps. The discovery of CNTs by Sumio Iijima [34] has been of significant importance in the aerospace and automobile industries in particular. Depending on the application, selective manufacturing of CNTs is possible, using Chemical Vapor Deposition (CVD), Carbon Arc Discharge method, Pulsed Laser Vaporization/ Laser Ablation and others [35-37]. Figure 2.4 [38] shows the schematic of different possible configurations of rolled graphene layers.

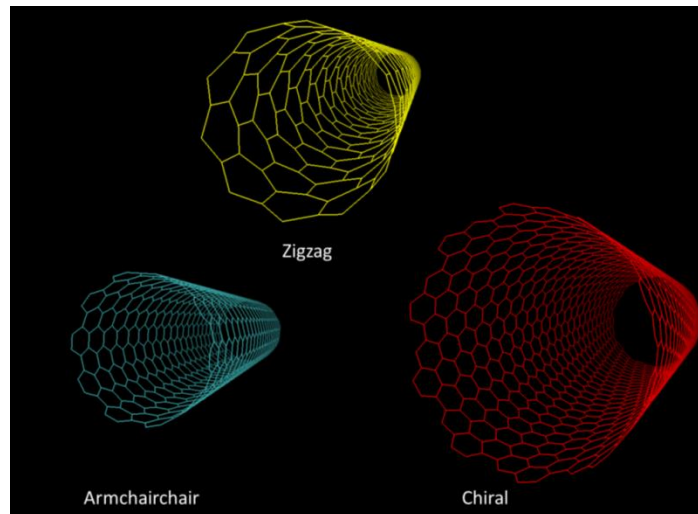


Figure 2.4: Schematic of Carbon Nanotubes Showing Folded Layer of Graphene

CNTs exist in various topological forms by the number of the cylinders that can vary from single-walled CNTs (SWCNTs), double-walled CNTs (DWCNTs) up to generic multi-walled CNTs (MWNTs), depending on its fabrication process. CNTs exhibit excellent mechanical properties. Tensile modulus of Single Walled Carbon Nanotubes (SWNTs) has been

reported to be around 1TPa and a tensile strength of 100 GPa [39]. CNTs have diameters ranging in nanoscale and lengths that could exceed up to millimeters, provides the CNTs with high aspect ratio. This results in high surface area which provides an excellent reinforcement for the polymer matrix [40]. This has made CNTs highly desirable in structural or multifunctional applications. Their high strength-to-weight ratio has provides a significant advantage as nano-fillers in modern-day composites and have been extensively incorporated in the modern day industries.

Both SWNTs and MWNTs have been used as reinforcement for both thermoset and thermoplastic polymers (as discussed in the next section). Nanocomposites consisting of DWNTs with high degree of dispersion, have showed increase strength, Young's modulus and strain failure with nanotube content of about 0.1 wt% [5, 41] and have also enhanced the fracture toughness of the baseline epoxy. Apart from mechanical properties, CNT/Polymer nanocomposites have also shown improvement in the thermal conductivity, by increasing the conductivity to 70% at 40 K and 125% at room temperature on adding 1 wt% [42] SWNT to the epoxy and 300 % increase on adding 3 wt% [43].

2.2 CARBON NANOTUBE REINFORCED FIBER COMPOSITES

2.2.1 Background:

Failure in fiber reinforced polymer matrix composites usually occurs in one of the three primary modes, fiber micro buckling, fiber fragmentation/fracture, matrix fracture, fiber-matrix interface delamination. Since the load transfer takes place through the interface region between the matrix and the fiber and the matrix is primarily responsible for carrying shear loads, it is very important to understand and improve this region for enhanced mechanical properties. Therefore, to improve interfacial strength, it is key to modify the polymer matrix, fiber and the interface.

Using Raman spectroscopy, Huang et al. [44] determined the distribution of interfacial shear stress along a single carbon fiber in thermoplastics and hence reported interfacial micromechanics of carbon fiber. The linear variations of the fiber strain with the position along its length indicated that the stress transfer from matrix to fiber is dominated by frictional shear. It was also reported that the maximum interfacial shear strength of polymethyl methacrylate (PMMA) and polycarbonate (PC) composites, which are known thermoplastics, was much lower than that of carbon fiber reinforced epoxy (thermosets) based polymer matrix. The high values of interfacial shear stresses of thermoset polymer matrix systems were attributed to the excellent chemical bonding between the fiber and the matrix systems.

In recent years, considerable effort was made to enhance this interfacial shear strength (IFSS) of CFRP composites. Using surface treatment to modify carbon fiber has been reported to increase the interlaminar Shear Strength (ILSS) [45-47]. One of the widely used methodology involved grafting of carbon nanotubes on glass or carbon fibers [22, 23, 27, 40, 48-50]. Coating CNTs on carbon fibers embedded in epoxy matrix, using single fiber fragmentation method has

also shown improvement in the interfacial shear strength [19]. On aligning CNTs on carbon fiber radially, an increase of 11% in the IFSS was recorded and on randomly aligning them an increase of 71% was recorded [21]. It was observed that on randomly aligning the CNTs, there was a high percentage of CNTs that were aligned at $\pm 45^\circ$ to the principal stress directions under pure shear loading, which gave the higher IFSS. However, a significant drop in the ultimate tensile strength and modulus was also reported in their findings. On the contrary, Sharma et al. [51] reported an improvement of 69% in the tensile strength when CNTs were grown on carbon fiber. Introducing low volume fraction of about 0.25% of MWNTs in the carbon fiber-epoxy composites resulted in an enhancement of 27% in the ILSS and also improved the out-of-plane electrical conductivity. Zhao et al. [52] also grafted Polyheral oligomeric silsesquioxanes (POSS) on carbon fibers. Using POSS is an emerging technology for nano reinforced organic-inorganic hybrids, which have increased the interlaminar shear strength by almost 61%.

Other approaches to introduce CNTs in the interfacial region between the epoxy and the carbon fiber have also been incorporated. One of them is to disperse regular and functionalized CNTs in the epoxy resin which has also been reported to significantly improve the IFSS [53-59]. Dispersion of CNTs in thermoset and thermoplastic resins has also shown improvement in the thermal as well as electrical conductivity [60, 61]. Some groups have also used carbon nanotube fiber to evaluate the IFSS [62-64] Bekyarove et al. [65] dispersed SWNT-COOH in epoxy to infiltrate carbon fiber by using vacuum assisted resin transfer modeling method to model a SWNT-COOH-epoxy-carbon fiber interface. On performing mechanical tests on these composites, an enhancement of 40% in the shear strength was recorded for just 0.5 wt% of SWNT-COOH. Two different groups of Tsotsis T. K. et al. and Fan Z. et al. [66-68], fabricated a hybrid MWNT-epoxy-glass fiber composite and reported an increase in the ILSS up to 33%.

Tseng et al. [69] and Cheng et al. [66] functionalized CNTs by plasma modification and prepared covalent-integrated epoxy composites which showed improvement in the tensile strength and the electrical conductivity. Godara et al. [24, 70] introduced carbon nanotubes to unidirectional epoxy-glass fiber macro-composite and performed single fiber push-out microindentation tests, which resulted in the increase of IFSS and also proved that the functionalized Double walled carbon nanotubes (DWNTs) are more effective than Single walled carbon nanotubes (SWNTs) because of the better alignment of polymer chains along the CNTs in axial direction. This was also validated by Barber et al. [71, 72], who proved the increase in the interfacial strength between single CNT and polymer when the surface of the nanotube was chemically modified. Improvement in the IFSS have also been reported through various other methodologies used by different groups on reinforced polymer composites using glass or carbon fibers embedded in thermoplastics, thermosets and metal matrices [73-76].

This dissertation follows the unique methodology of carbon nanotube aerogel sheet being circumferentially scrolled around carbon fiber tow to improve IFSS embedded in BMI epoxy resin [77]. Figure 2.5 shows a transmission electron microscopy (TEM) image of MWNTs and 2.6 shows the procedure of MWNT sheet pulled out from a forest.

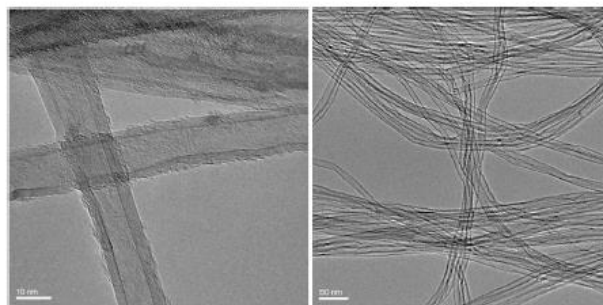


Figure 2.5: TEM images of MWNT (Courtesy: Alan G. McDiarmid Nanotech Institute, UT Dallas)

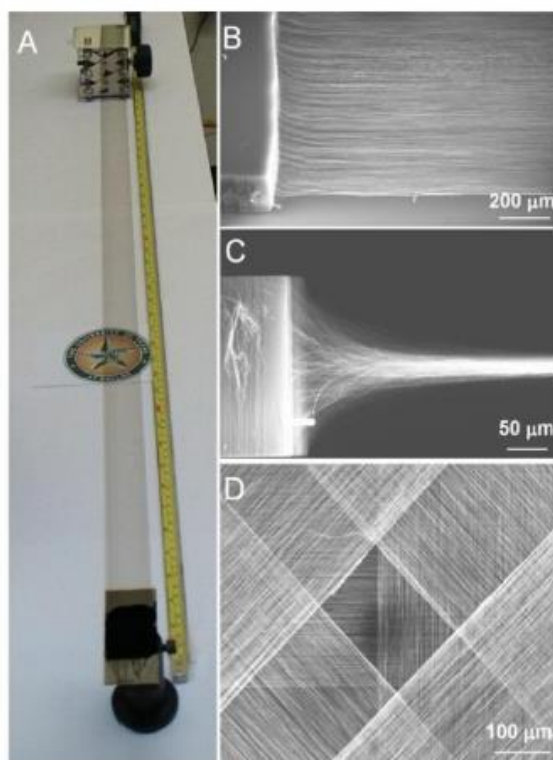


Figure 2.6: MWNT Forest Conversion into Sheets and Assembly into Sheets a) 0.34 m Wide, 1 m Long MWNT Sheet, b) SEM Image of MWNT Forest Drawn into Sheet, C) SEM Image of Cooperative 90° Rotation of MWNT Forest into a Sheet, D) SEM Image of 2-D Reinforced Structure Fabricated by Overlaying Four Nanotube Sheets with 45° Shift in Orientation between Successive Sheets (Zhang et al.[78])

2.2.2 Carbon Nanotube Sheet Scrolled Carbon Fiber In Polymer Composites

Mohammed et al. [77] used drawable MWNT forest, grown using chemical vapor deposition (CVD), of diameters of about 10 nm with six walls. The highly oriented MWNT sheets were fabricated by drawing them from MWNT forest, which had a density of ~ 1.5 mg/cm³, and a high specific strength of 144 MPa·cm³/g. PAN based carbon fiber with diameter of 5.2 μm and density of 1.78 g/cm³ was used, with tensile strength of 5.31 MPa and modulus of

276 GPa. Two different epoxy materials were used, Loctite Epoxy and BMI Matrimide resin system.

The MWNT sheet was then scrolled circumferentially on the carbon fiber at a wrapping angle α (as shown in Figure 1.2) and then was embedded in the polymer matrix. This specimen was then subjected to fiber pull-out test and fiber push-out test to calculate the interfacial shear stress using the following equation:

$$IFSS = \frac{P}{\pi dl} \quad (2.1)$$

where P was the applied load (pull-out or push-out), d is the fiber diameter and l is the fiber length embedded in the matrix. Figure 2.7 shows the pull out and push out force plotted as a function of displacement for neat carbon fiber embedded in epoxy as compared with the MWNT sheet scrolled carbon fiber embedded in epoxy. This figure clearly shows the improvement in the peak load on wrapping the carbon fiber with MWNT sheets.

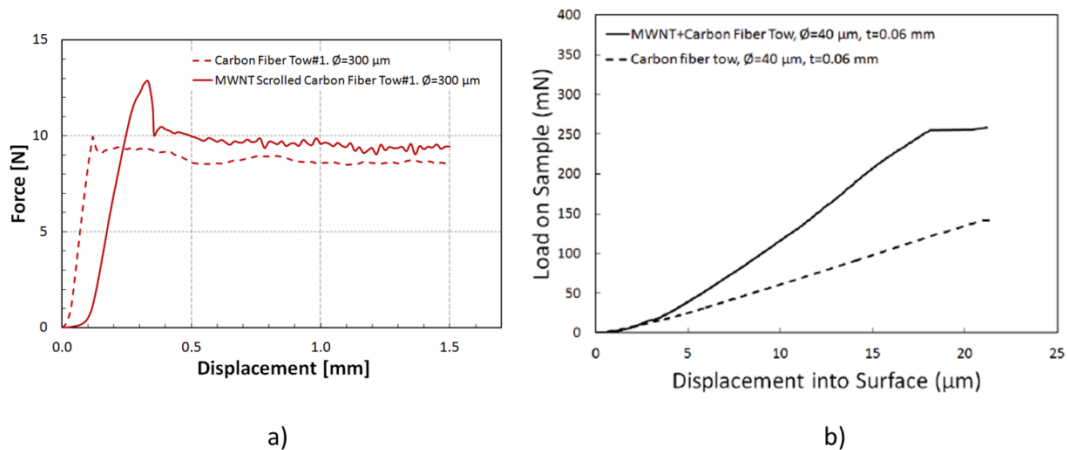


Figure 2.7: a) Load Vs Displacement in Pull-Out Tests for 300 μm Tow With and Without Scrolled MWNT, b) Load Vs Displacement Plots for Push Out Tests for Carbon Fiber Tow With and Without Scrolled MWNT (Courtesy: Haque MH [77])

From these tests, Mohammed et al. [77] showed significant improvement in the interfacial shear strength when carbon fiber tows were circumferentially scrolled with MWNT sheet. The macroscale pull out test, using tensile testing machine showed an improvement of about 31% in the IFSS and the microscale push out test, using nanoindentation showed an improvement of 81% in the IFSS.

This method was different from previous experiments where carbon nanotubes were grown or grafted on the individual carbon fiber in the following ways:

- The conventional practice of growing CNT on carbon fiber required high temperature for the dissolution of catalytic particles on the carbon fiber surface, which would degrade the carbon fiber properties, specifically its in-plane properties. This method could be performed at room temperature, hence avoiding the high temperature degradation.
- This method provided higher surface contact area between the carbon nanotube and the carbon fiber, generating enhanced interfacial bonding.
- It also provides higher surface contact area between the polymer matrix and the CNT, hence reinforcing the matrix, and improving its load bearing capabilities.
- This method is up-scalable compared to conventional methods.

2.3 MULTISCALE MODELING

To avoid uncertainty and reduce risk in the variations in the constituent materials of Polymer Matrix Composite (PMC), the processing, the manufacturing process and end-use scenarios of performance and failure of a component, requires extensive testing, before being incorporated into the Design Allowable Database. This is a major limitation in using new and improved PMC. The development of Design Allowable Database involves analysis of multiple composite batches including the associated construction of large mechanical and physical properties. Further, expensive fabrication process of the numerous subcomponents and expensive testing of these components, to verify the long term performance. All the addition time and costs participating in these processes are heightened through complications due to large error bands in the properties, processing complications or tooling rework.

To overcome these issues, Integrated Computational Materials Science and Engineering (ICMSE) methodology provides material development by avoiding expensive trial-and-error approach of material fabrication and characterization. A multiscale physics based modeling approach, is necessary to accurately design and study the material anisotropy. This approach allows analyzing the individual constituents to their basic structure and their roles in the interface region, and hence to accurately predict the response of PMC aircraft structures and their mechanical response. Figure 2.8 depicts the length scales involved in this multiscale approach, where, atomistic (nanoscale) simulations provide input data for the micro-mechanical response, which is further used as the input for a three-dimensional ply-level analysis, which includes the spatial variability of material properties and thereby the multi-functionality in the composite structure. This accounts for the ply-level mechanical properties and can be used to predict the

failure initiation in the aircraft structure [79, 80]. In the following chapter, the molecular dynamics theory, force fields available and used, the MD software used for the nanoscale simulations and other concepts are discussed.

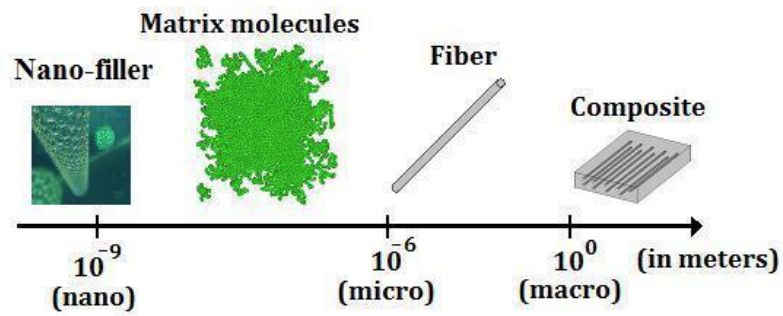


Figure 2.8: Length Scales Involved in the Multiscale Modeling

2.4 MOLECULAR DYNAMICS SIMULATIONS

2.4.1 Introduction

Molecular Dynamics (MD) simulations are based on Newtonian mechanics to simulate the physical interactions of a system at the atomic level. From being used to study the interactions of hard spheres during the 1950's [29] to the study of water, subsequently to simulate proteins and for other biological applications over the years, MD has come a long way, to being efficiently used to simulate and predict nano-scale atomic and molecular interactions . MD makes use of Newtonian equations of motions to solve the motion of every particle or atom in an N-particles system and hence provide the resulting physical state of the system.

$$m_i \ddot{x}_i^t = - \frac{\partial V(x_1^t, x_2^t, \dots, x_N^t)}{\partial x_i^t} \equiv F_i^t \quad (i = 1, 2, \dots, N) \quad (2.2)$$

This classical equation of motion is used in the molecular dynamic simulations to represent an atomic system, where the change of motion is proportional to the applied force to the object (Second Law). The potential energy (V) in equation (2.2), depends on the force field, is used to compute the internal force, F_i for any atom i , of mass m_i and position x_i [$x^t = (x_1, x_2, \dots, x_N)$ represents the complete set of $3N$ atomic coordinates].

2.4.2 Algorithms

The calculation of total force on each particle and subsequently the calculation of new positions and velocities of each atom in the molecular system is a complex procedure due to complexity of the potential functions. To overcome this, numerical integration methods are used to integrate the equations of motion and determine the updated positions and velocities of the atoms [81]. These algorithms use a Taylor series expansion to approximate the position and dynamic properties of the system. Depending on the function of the MD simulation, the algorithm used to run the simulation can be chosen based on the following criteria:

- The algorithm should be able to conserve the energy and momentum of the system
- The algorithm should be computationally efficient
- Should allow long timestep for integration
- Should be able to approximate the classical trajectory as closely as possible

Some of the commonly used algorithms used in MD simulations are discussed below:

I. **VERLET ALGORITHM:** In this method, the positions ' r ' and acceleration, ' a ' of the atoms at time ' t ' along with the positions at time ' $t-\Delta t$ ' are used to calculate the new position at time ' $t+\Delta t$ ' [82]. Using the Taylor Series Expansion, position at time ' $t+\Delta t$ ' and ' $t-\Delta t$ ' can be written as,

$$r(t + \Delta t) = r(t) + v(t)\Delta t + \frac{1}{2} a(t)\Delta t^2 \quad (2.3)$$

$$r(t - \Delta t) = r(t) - v(t)\Delta t + \frac{1}{2}a(t)\Delta t^2 \quad (2.4)$$

where ‘ v ’ is the velocity of the atoms. Taking the sum of the two equations, the updated position in terms of previous position and accelerations can be written as,

$$r(t + \Delta t) = 2r(t) - r(t - \Delta t) + a(t)\Delta t^2 \quad (2.5)$$

From the equations (2.3-2.5), it should be noted that the explicit computation of the velocities is not required. This algorithm is relatively simpler and the computation is resource friendly, however, the method is not very accurate [83].

II. LEAP-FROG ALGORITHM: This method tries to overcome the short comings of the Verlet algorithm [84] [85]. And one of the ways that this algorithm uses to do so, is by explicit computation of the midstep velocities ‘ v ’ at time ‘ $t + (1/2)\Delta t$ ’ given by equation (3.5). Even though this method has the advantage of explicit computation of velocities, the positions and velocities are calculated at different times.

$$v(t + \frac{1}{2}\Delta t) = v(t - \frac{1}{2}\Delta t) + a(t)\Delta t \quad (2.6)$$

The positions ‘ r ’ at time ‘ $t + \Delta t$ ’ can be computed as,

$$r\left(t + \frac{1}{2}\Delta t\right) = r(t) + v\left(t + \frac{1}{2}\Delta t\right)\Delta t \quad (2.7)$$

Velocities ‘ v ’ at time ‘ t ’ are thus given by,

$$v(t) = \frac{1}{2} \left(v\left(t - \frac{1}{2}\Delta t\right) + v\left(t + \frac{1}{2}\Delta t\right) \right) \quad (2.8)$$

III. BEEMAN’S ALGORITHM: Similar to Verlet algorithm, this method produces identical positions, but uses different formula for velocities [86, 87]

$$v(t + \Delta t) = v(t) + \frac{3}{2}a(t)\Delta t - \frac{1}{6}a(t - \Delta t)\Delta t \quad (2.9)$$

$$r(t + \Delta t) = r(t) + v(t)\Delta t + \frac{2}{3}a(t)\Delta t^2 + a(t)\Delta t^2 \frac{1}{6}a\left(t - \frac{2}{3}a(t)\Delta t\right)\Delta t^2 \quad (2.10)$$

This method is more accurate to calculate the velocities, and for better energy conservation, but comes with a higher computational cost.

IV. VELOCITY VERLET ALGORITHM: This is one of the most commonly used algorithm for MD simulations. This method is a variant of the Verlet algorithm, but produces more precise and accurate positions and velocities of the atoms [88] as shown in equation 2.11 and 2.12. Here, $r(t \pm \Delta t)$ is the position vector and $v(t \pm \Delta t)$ is the velocity vector and $a(t)$ is the acceleration vectors of the atoms in different time directions

$$r(t + \Delta t) = r(t) + v(t)\Delta t + \frac{1}{2}a(t)\Delta t^2 \quad (2.11)$$

$$v(t + \Delta t) = v(t) + \frac{1}{2}(a(t) + a(t + \Delta t))\Delta t \quad (2.12)$$

2.4.3 Ensembles, Thermostats and Barostats

I. ENSEMBLES

In the terms of statistical mechanics, an ensemble average can be defined as the mean of a quantity that is a function of the microstate of a system. Generally, there are four different types of ensembles in MD simulations:

a) Microcanonical Ensemble (NVE): This is an adiabatic type of thermodynamic state, where the Number of atoms (N), Volume (V) and the Energy (E) of the system are fixed during the simulation. No exchange of heat is specified in this type of ensemble, and hence it relates to an isolated system where the total energy of the system is conserved.

b) Canonical Ensemble (NVT): In this ensemble, the Number of atoms (N), the Volume (V) and the Temperature (T) are specified by the user and conserved during the simulation. This type of the ensemble represents a heat bath, where the system is maintained in a thermal equilibrium at a specified temperature. A thermostat can be used to add or remove energy from the system.

c) Isothermal-Isobaric (NPT): In this type of ensemble, along with the Number of atoms (N), the Pressure (P) and the Temperature (T) of the system are kept constant, by making use of

thermostats and barostats. In this case, to achieve the state of constant temperature and pressure within a given window, the change in the volume of the system is allowed.

d) Isoenthalpic-Isobaric (NPH): This ensemble, keeps the Number of atoms (N), the Pressure (P) and the Enthalpy (H) of the system, constant. The enthalpy (H) of a homogeneous system, as shown in Equation 3.12, is maintained constant by varying the volume (V), and Internal Energy (U). Here p is the Pressure of the system

$$H = U + pV \quad (2.13)$$

II. THERMOSTATS

A thermostat algorithm is a modification of the Newtonian MD scheme that generates a thermodynamically ensemble at constant temperature. The use of thermostat can be motivated by either or a number of the following reasons:

- To preserve experimental conditions.
- Maintain realistic dynamics in the equation of motion to compute the transport qualities accurately.
- To study temperature dependent processes
- To evacuate the heat in dissipative non-equilibrium MD simulations
- From statistical mechanics, the temperature (T) of the system is defined by the average of Kinetic Energies (K) of all particles [89]. For a system of N particles, the temperature of the system is given by:

$$T = \frac{2\langle K \rangle}{3Nk_B} \quad (2.14)$$

k_B is the Boltzmann's constant, and $\langle K \rangle$ implies the average of the Kinetic Energy over an ensemble. Here, the average of the kinetic energy is considered since, it is difficult to maintain a constant temperature of the system because of the fluctuations in the atomic velocities in the system, throughout the simulation. Hence only the average value of the temperature of the system is maintained. As it is evident from Equation (3.13), the temperature of the system depends on the Kinetic Energy of the particles, which in turn is influenced by the velocities of the atoms. A common method to control an average temperature is to use velocity rescaling. However, this approach does not capture the correct energy fluctuations in the system. So, different thermostats are made use of, to facilitate the finite temperature changes in the system. Some of the most commonly used thermostats are discussed below:

a) Berendsen Thermostat: The Berendsen thermostat [90] uses the same approach as velocity rescaling, but assigns a time scale for updating the velocities, and unlike the velocity rescaling approach, where the velocities are completely scaled to the target temperature at each time step. In this approach, it is assumed, that the system is weakly coupled to a heat bath at the desired temperature. This thermostat does not capture the energy fluctuations correctly, and faces the same issues as velocity rescaling.

b) Anderson Thermostat: The Andersen thermostat [91] makes use of random collisions of molecules with an imaginary heat bath at the desired temperature, that introduces a

stochastic element to the temperature. The time between the collisions is randomly decided. In the single-particle approach, at a desired temperature, a randomly chosen particle and its velocity is reassigned from a random Maxwell-Boltzmann distribution. There is an alternative approach, where a massive collision can be used in which each velocity component of every particle in the system is reassigned simultaneously.

c) Nose-Hoover Thermostat: Initially developed by Nose [92] and later improved by Hoover [93], this type of thermostat is one of the most accurate and computationally efficient approach, widely used for MD simulations, for temperature control. This thermostat, uses a heat bath to add an artificial variable ' s ', a velocity ' \dot{s} ' to the system and with an associated mass ' Q ', which also determines the extent of coupling between the MD system and the heat bath. This approach does not need time scaling by s . This algorithm fails to generate a canonical distribution for a single harmonic oscillator. This shortcoming has led to the need for developing newer thermostating algorithms.

III. BAROSTATS

It is often required to maintain constant temperature and pressure for simulated system. Thermodynamically, maintaining a constant temperature and pressure can result in fluctuating volume of the system. Several barostat techniques are available to achieve the desired pressure by readjusting the volume of the MD system. Some of the commonly used barostat techniques used in MD simulations are:

- Volume Rescaling – by rescaling the volume of the system at periodic intervals, the target pressure is achieved.
- Berendsen Barostat – the pressure of the system is coupled to a “pressure bath” which in turn rescales the volume.
- Extended Ensemble Barostat – Like the Nose-Hoover thermostat, this barostat uses an extended Lagrangian and new degrees of freedom, and couples a “pressure bath” to maintain the constant pressure in the MD system.

2.4.4 Boundary Conditions:

Finite systems behave very differently from that of the infinite or massive systems [94]. Simulating small clusters of atoms or molecules with well-defined number of constituents would not help in obtaining the bulk properties of macroscopic systems from MD simulations. Hence, the number of particles used in the MD system for simulation purposes plays a key role. Regardless how large system we choose with N number of particles in our simulations, it would still be negligible from a macroscopic point of view.

The MD systems comprise of a very small fraction of atoms located near the boundary or the walls from a macroscopic stand. Therefore, in large systems, the fraction of particles near the walls is negligible. However, the fraction of the surface atoms in an MD system is much more significant, the behavior would be affected by the surface effects or the edge effects [95, 96]

To resolve both these issues, of finite size and to reduce the surface effects, it is very common to use *Periodic Boundary Conditions*. Using periodic boundary conditions on the MD system, basically implies that the number of particles enclosed in our simulation box is repeated infinitely by rigid translation in every Cartesian direction, occupying the space, as shown in

Figure 2.9 [97]. Periodic boundary conditions create “image” particles in all the directions of periodicity and moves solitary with their “original” particle from the simulated box. When a particle leaves or enters the simulation region, an identical “image” particle enters or leaves this region, thus maintaining the same number of particles as in the MD system. This removes any surface effects and the position of the box boundaries have no effect on the properties.

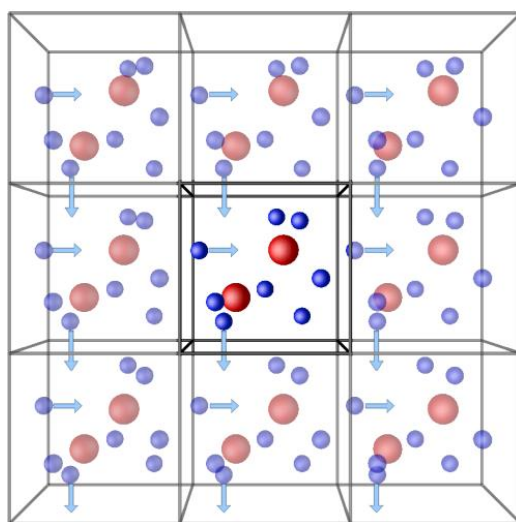


Figure 2.9: Schematic of a System with Periodic Boundary Conditions (Courtesy: Central Michigan University [97])

2.5 FORCE FIELD POTENTIALS

2.5.1 Introduction

Computer simulations have evolved as a powerful tool to study the dynamics and structural properties of various systems. Detailed molecular structures and interactions can be predicted using quantum mechanics (QM) methods. However, to study large molecular systems, these methods required high computational costs. Hence, development of simplified approximations was necessary to investigate larger systems. The potential functions make use of Born-Oppenheimer approximation to reduce the full quantum description, to write the energy of the system as a product of mutually independent functions of nuclear and electron coordinates [98]. The nuclei of the atoms are treated as point particles which follow Newtonian dynamics. The position and the configuration of the electrons within the atom's shell are ignored and the potential functions use the energy due to the position of the nuclei with respect to each other. This allows the MD simulation of large molecular systems. The MD algorithms, as discussed in previous sections, use these force fields in general empirical fits to quantum mechanical calculations, and in certain cases provides results as accurate as the highest quantum mechanical calculations [98].

A force field is a set of mathematical expressions that defines the energy of a system depending on the coordinates of its particles. It is based on a set of parameters entering the mathematical form and the analytical form of the interatomic potential energy. The parameters are obtained from various methods like, *ab initio* or semi-empirical quantum mechanical calculations or by making use of fitting experimental data from neutron, X-ray and electron diffraction, NMR, Raman spectroscopy etc. The atoms in the MD system are held together by

simple elastic (harmonic) forces and the force field replaces the true potentials with a simplified model depending on the purpose of the MD simulations. There are several force fields available for different kinds of systems in question for analysis, and with different degrees of complexity. The type of molecular system that is to be used in the simulation, decides the exact functional form and parameters of the potential function. But, all the force fields are based on a typical expression as shown in equation (2.15).

$$\begin{aligned}
 U = & \sum_{bonds} \frac{1}{2} k_b (r - r_0)^2 + \sum_{angles} \frac{1}{2} k_a (\theta - \theta_o)^2 + \sum_{torsions} \frac{V_n}{2} [1 + \cos(n\phi - \delta)] \\
 & + \sum_{improper} V_{imp} + \sum_{LJ} 4 \epsilon_{ij} \left(\frac{\sigma_{ij}^{12}}{r_{ij}^{12}} - \frac{\sigma_{ij}^6}{r_{ij}^6} \right) + \sum_{elec} \frac{q_i q_j}{r_{ij}}
 \end{aligned} \tag{2.15}$$

Here, k_b k_a are the force constants, r is the distance between two bonded atoms, r_0 is the equilibrium bond distance, θ is the bond angle between two bonds, θ_o is the equilibrium bond angle, ϕ is the torsional angle, δ is the phase, n defines the number of maxima or minima between 0 and 2π , V_n is the height of the potential barrier, V_{imp} is the improper torsion. In this equation, the total energy of the system is calculated, where the first four terms refer to the local or intramolecular contributions from bonds stretching, angles bending, dihedral and improper torsional energies, and the last two terms describe the energies from the van der Waals interactions (in this case by means of 12-6 Lennard-Jones potential) and the Coulombic interaction.

The potential functions play a critical role in molecular dynamics simulations. Defining the correct potential function is very crucial since, the potential functions determine the

acceleration of the atoms or particles, which is then used to update the positions and the velocities of all the atoms or particles in the system. There are many force fields available in literature, resourceful for simulating various types of systems. Traditionally, force fields with fixed bond topologies were used to model covalent systems by defining the bonds at the beginning of the simulation and remain fixed throughout. Some of the common force fields used in such methodologies are, AMBER, OPLS, CHARM and COMPASS. The MD systems modeled using such force fields with their corresponding assumptions have been analyzed and proven to be appropriate for systems like polymers and proteins. However, these force fields are not adaptable to reactive systems, and they are not able to replicate the bond breakage and/or bond formation reactions in the MD system. So, to overcome this, reactive force fields are suggested to be used for material research, which allows us to study crack-formation, propagation and fracture. Reax Force Field (ReaxFF) is a reactive force field based on the bond order, developed by Adri van Duin et al. [99]. In this dissertation, three types of potential functions are analyzed and discussed, OPLS, FENE and ReaxFF.

2.5.2 OPLS

The Optimized Potentials for Liquid Simulations (OPLS) force field was developed by William Jorgensen [100] and is a widely used potential function for simulating polymer materials[101-104]. OPLS potential function makes use of predefined information of the molecular structure, including both bonded and non-bonded arrangements of the atoms in the molecular system. The OPLS force field uses the sum of the energies from the bonded and the non-bonded interactions, to calculate the total energy of the system, E as shown in Equation (2.16)

$$E_{Total} = E_{bonded} + E_{non-bonded} \quad (2.16)$$

The energies due to the bonded interactions is usually defined as the sum of the energies due to the bonds, angles and dihedral. And the total energy of the system can be re-written as:

$$E_{Total} = E_{bonds} + E_{angles} + E_{dihedrals} + E_{non-bonded} \quad (2.17)$$

I. BOND ENERGY

The extension or compression of the bonds between two atoms and the energy associated with the bond stretching due to those effects, accounts for the contribution as the bond energy in the total energy of the system. Equation (2.18) uses harmonic potential to describes the simplest form of the bond energy

$$E_{bonds} = \sum_{bonds} K_b (r - r_o)^2 \quad (2.18)$$

Here, K_b is the bond stiffness, r is the current bond length (at a particular timestep), and r_o is the original bond length or the equilibrium bond length. All the bonds in the system are accounted for while calculating the bond energy contribution in the total energy.

II. ANGLE ENERGY

Because of the atomic movements during a MD simulation, just like how the bonds stretch, the angles between the atoms can change from their equilibrium configurations. The energy contributions due to the change in angles is described as in equation (2.19)

$$E_{angles} = \sum_{angles} K_\theta (\theta - \theta_o)^2 \quad (2.19)$$

Here, K_θ is the stiffness constant, θ is the current angle between three bonded atoms and θ_o is the equilibrium angle.

III. DIHEDRAL ENERGY

The change in the shape due to environmental and other factors, contributes to the flexibility and dynamic behavior of the polymers. Each possible shape is called a confirmation and the transitional change between these shapes is called the conformational change. In polymers, the conformational changes are primarily due to the complexity between the torsional and non-boded interactions. Due to the repulsive forces between the non-bonded interactions between the end atoms of the torsional unit, act as a limitation to the rotation between the

chemical bonds. These energy restrictions in the rotation about chemical bonds define the structure property of the polymer and are expressed using a cosine series expansion [100-104], as shown in Equation (2.20)

$$E_{dihedrals} = \frac{1}{2} K_1 (1 + \cos(\phi)) + \frac{1}{2} K_2 (1 - \cos(2\phi)) + \frac{1}{2} K_3 (1 + \cos(3\phi)) + \frac{1}{2} K_4 (1 - \cos(4\phi)) \quad (2.20)$$

Here, K_1 , K_2 , K_3 , K_4 , are constants in the series, ϕ is the dihedral angle as shown in Figure 2.10.

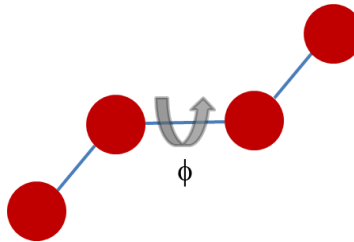


Figure 2.10: Schematic of Dihedral Angle

IV. NON-BONDED INTERACTIONS

Non-bonded interactions act between atoms that are not linked by covalent bonds. The two main contributors to the energies due to non-bonded interactions are electrostatic interactions and van der Waals interactions. The handling of electrostatic interactions is slightly more complicated and depends on the charges on the nuclei and the electrons of the atoms, which is governed by the Coulomb's law:

$$V = \frac{q_i q_j}{4\pi\epsilon_0\epsilon_r r_{ij}} \quad (2.21)$$

where, q_i and q_j are the magnitude of the charges, r_{ij} is the distance between them, ϵ_r is the relative dielectric constant of the medium in which charges are placed and ϵ_0 is the permittivity of free space.

However, it's the van der Waals forces that are the major source of the energy contributions in the non-bonded interaction between atoms and molecules in a system. Named after the famous Dutch scientist, Johannes Diderik van der Waals, these forces are distance dependent interactions between atoms, which is the sum of the attractive and repulsive forces between atoms and molecules in the system. Because of these forces being short range nuclear forces, the influence zone for these forces to make an influence is in the range of few Angstroms. The attractive component of the forces, called the London dispersion forces, is a temporary attractive force, results when the temporary dipoles are formed when the electrons in two adjacent atoms occupy the required positions. Because of this action, this type of force is also called the induced dipole- dipole attraction. The repulsive forces, on the other hand, are affected by the Pauli Exclusion Principle. The theory behind the repulsive forces, if affected by the electrons or the nuclei is debatable, but either ways, no two atoms can get too close to each other without experiencing repulsive forces. Both attractive and repulsive forces contribute to the van der Waals forces, and are based on the interatomic distance, as shown in Figure 2.11.

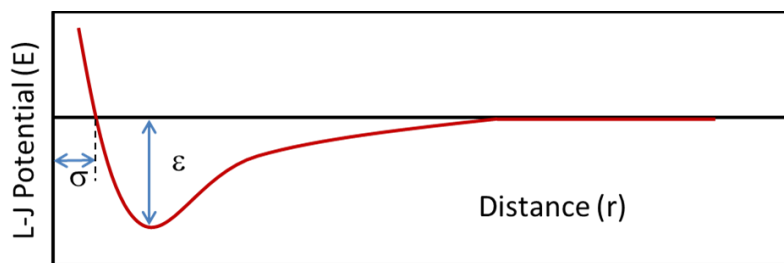


Figure 2.11: Variation in L-J Potential with Inter-Particle Distance

The empirical potentials used to define these non-bonded potentials is called the Lennard-Jones (L-J) potentials and is expressed mathematically as:

$$E_{non-bonded} = 4\epsilon \left[\left(\frac{\sigma}{r} \right)^{12} - \left(\frac{\sigma}{r} \right)^6 \right] \quad (2.22)$$

here, ϵ is the depth of the potential well, σ is the finite distance at which the inter-particle potential is zero, r is the interatomic distance.

2.5.3 ReaxFF

Traditional potential functions like OPLS are much simpler to use and are computational friendly, but they are unable to simulate chemical reactions since they lack the capability to simulate bond formation and bond breakage between the atoms. However, more recent potential functions like Reactive force field (ReaxFF), which is a bond order based force field, allows continuous bond breakage and formation [99], and suits more closely to simulate material behavior under sustained loading. This advantage is used to serve the purpose of this dissertation more relevantly. ReaxFF uses the bond distance-bond order relationship on one hand and the bond order-bond energy relationship on the other, to simulate the proper dissociation of bonds to

separated atoms. Valence terms like angle and torsion, present in the force field are also defined in terms of the same bond orders, which when the bonds break, goes to zero. Non-bonded interactions between the atoms, like van der Waals and Coulombic potentials, are also taken into consideration in the ReaxFF force field, thereby incorporating all the interactions presents in the system. The ReaxFF parameters are derived from quantum chemical calculations on bond dissociation, reactions of small molecules, heat formation and geometry data of several stable hydrocarbon compounds.

Similar to the empirical force fields like OPLS, the total energy of the system is described by ReaxFF as a sum of various partial energies as shown in Equation (2.23).

$$\begin{aligned}
 E_{total} = & E_{bond} + E_{valence\ angles} + E_{overcoordination} + E_{undercoordination} \\
 & + E_{torsion} + E_{conjugation} + E_{Coulomb} + E_{vdWaals} + E_{penalty}
 \end{aligned}
 \tag{2.23}$$

Each of these partial energy terms is a function of bond order, which depends on the interatomic distance. The dependency of Bond Order between two atoms i and j , to the interatomic distance between them, can be described as:

$$BO_{ij} = \exp \left[p_{bo,1} \bullet \left(\frac{r_{ij}}{r_o} \right)^{p_{bo,2}} \right]
 \tag{2.24}$$

Here, $p_{bo,1}$ and $p_{bo,2}$ are the bond constants, r_{ij} is the current distance and r_o is the equilibrium distance between the atoms i and j . From this relationship between the bond order

and the bond distance, it can be said that the bond order decreases exponentially as the bond distance between the two atoms increase, as shown in Figure 2.12:

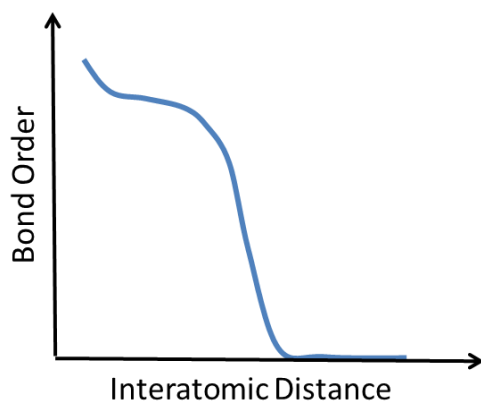


Figure 2.12: Schematic of Bond Order Relation with Interatomic Distance

All the partial energies are governed by the interatomic distance, which in turn simplifies the dynamic breakage and formation of the chemical bonds by computing the bond order.

2.6 SIMULATION PROCEDURE

As discussed earlier, Molecular Dynamics is a computational simulation technique which is used to study the motion of the atoms, using classical Laws of Physics, by allowing atoms and molecules to interact over a small time period. The information from the positions and velocities of atoms in a system over the course of a simulation, are collectively used to determine the statistically properties of the system. The mechanical, thermal, electrical as well as any other time dependent properties are determined based on the force field chosen to perform the MD analysis.

A classic MD simulation basically consists of a data file and an input file. The data file, is made up of the initial positions and the velocities of all the atoms in the system. And depending on the type of molecular system, may need to include other necessary information for all the atoms like the force field parameters, bond, angle, charges and dihedral information, etc. However, there are some potential functions like the Reax-FF potentials, where only the initial atomic positions and velocities are required in the data file, before the start of the simulation. All these information from the data file is read by the input file where the user defines various parameters for the simulation like the total simulation run time, ensembles (discussed in detail in later sections), deformations etc., according to the purpose of the simulation. Figure 2.12, shows a general algorithm followed by a typical MD simulation, where the input file reads the data file and follows the following steps to perform a simulation specified by the users.

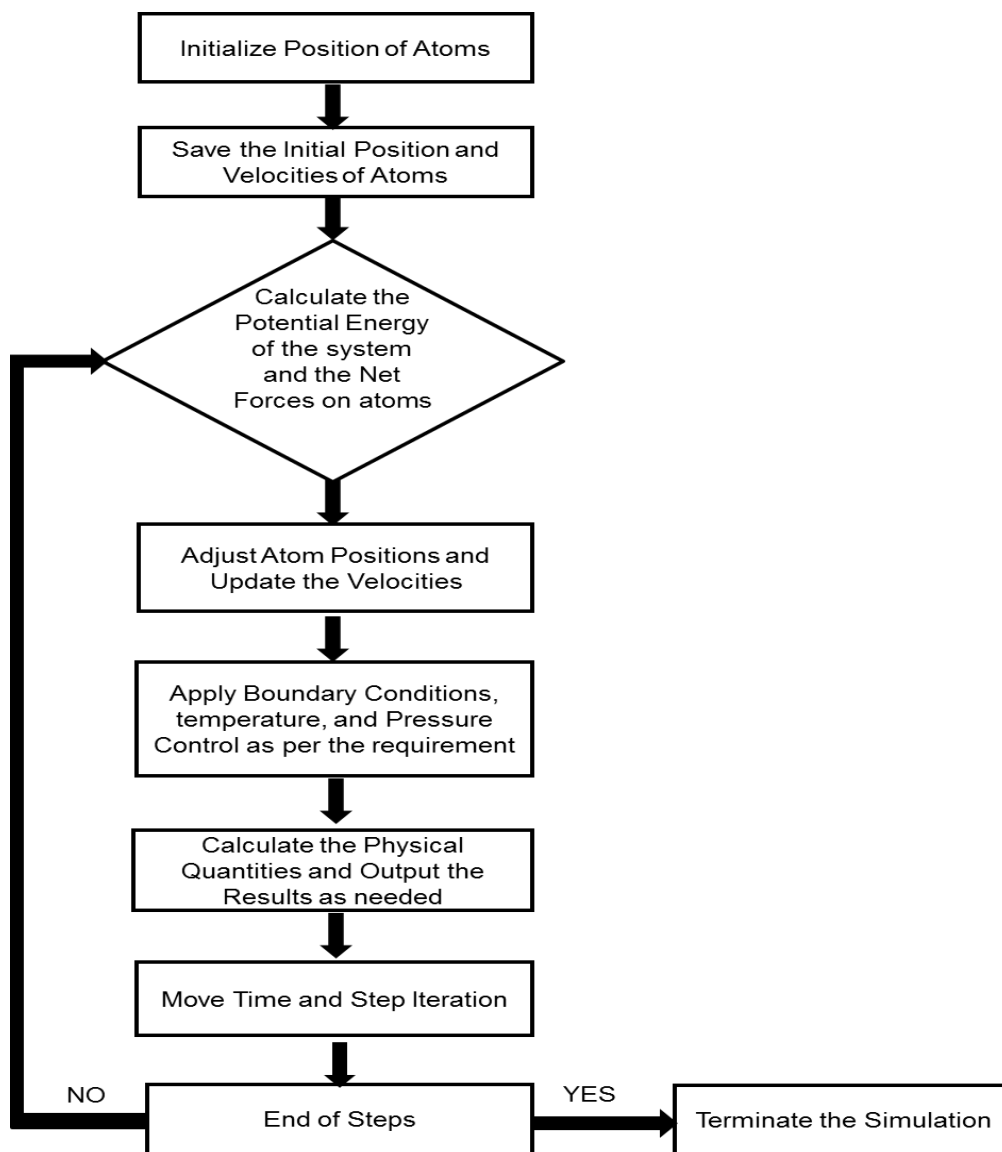


Figure 2.13: Algorithm of a Generalized Molecular Dynamics Simulation

Generally, before the start of any simulation, the initial data file or the initial system is brought to its minimum energy state by iteratively adjusting the atomic positions of the system. Once, an energy-minimized state is reached, the system is let to undergo the user defined simulation, where-in, various parameters like the temperature, pressure, volume etc. could be changed or set to a certain value. This lets to a change in the initial position and velocities of the system. Forces on every atom in the system are calculated (as shown in formula 3.1) and

Newton's Second Law is used to calculate the new positions and velocities of the atoms and are updated every timestep.

2.7 LAMMPS OVERVIEW

All the molecular dynamics simulations in this dissertation were performed using the Large Scale Atomic/Molecular Massively Parallel Simulator (LAMMPS), which was developed by Sandia National Labs [105]. LAMMPS is a classical MD code that allows modeling an ensemble of particles in a liquid, solid or gaseous state. It allows the user to model atomic, coarse-grained, granular, polymeric, biological and metallic systems with the help of variety of force fields and boundary conditions.

LAMMPS is based on integrating Newton's equations of motion for a collection or atoms, molecules or macroscopic particles that interact under different range of forces, along with initial and/or boundary conditions. LAMMPS keeps a track of nearby particles for computational efficiency, which also could be optimized to maintain the density of the particles. LAMMPS runs most efficiently on parallel computers using spatial-decomposition techniques.

LAMMPS uses an input script to read the atomistic data from a data file. The data file comprises all the information for every single atom in the MD system, like the position coordinates, velocities, bonds, angles, dihedrals, charges etc., depending on the type of simulation and force fields specified by the user. The input file is used to set the parametrization factors like the ensemble, thermostats, barostats and potentials on the MD system. The input script is also used to perform other actions like to apply deformations on the system, make changes in the model, and introduce any other element and many other actions. The timestep and

the number of run steps specified in the input script decides the outcome of the simulation, by allowing how well a system is equilibrated in the conditions specified and/or desired by the user. The output parameters from these simulations can be stored in different files, at different time intervals, again to be specified in the input File. LAMMPS just outputs numbers and has no way of graphically analyzing the output files. There are other visualization software available that can read the output files from LAMMPS and provide a graphical representation of the simulation.

2.8 OVITO

Open Visualization Tool (OVITO) is an open source scientific data visualization and analysis software that is used in all the graphical representation of the MD models, in this dissertation. Developed by Alexander Stukowski at Darmstadt University of Technology, Germany [106, 107], OVITO able to read and translate the numerical output from LAMMPS into graphical representations and allows the user to perform visual analysis of the large scale atomistic simulations like, color coding of atoms, bond analysis, slicing, tracking of particles etc. It's very simple software and supports multiple file formats and also can be used to export high quality images and animations.

CHAPTER 3

MULTISCALE MODELING METHODOLOGY FOR PREDICTING COMPRESSIVE STRENGTH ENHANCEMENT IN CARBON FIBER REINFORCED COMPOSITES USING SCROLLED MWNT SHEET

3.1 MULTISCALE APPROACH

3.1.1 Introduction:

To study the effect of multi-wall nanotube (MWNT) overwrapping on the mechanical properties of the carbon fiber reinforced polymer composites, such as compressive strength and interfacial shear strength, simulations were performed and verified with experimental results. A hierarchical multiscale approach was used to perform the nanoscale simulations to calculate the compressive strength of the carbon fiber composite with and without the MWNT overwrap. The hierarchical multi-scale model is schematically depicted in Figure 3.1, where molecular dynamics (MD) was used to generate nanoscale morphology of the interface region containing the epoxy matrix and the scrolled MWNTs, which was then incorporated in a microscale formula to calculate the shear modulus of the carbon fiber reinforced composite, and finally in a macroscale (Argon's) formula to predict the compressive strength of the carbon fiber reinforced polymer composite.

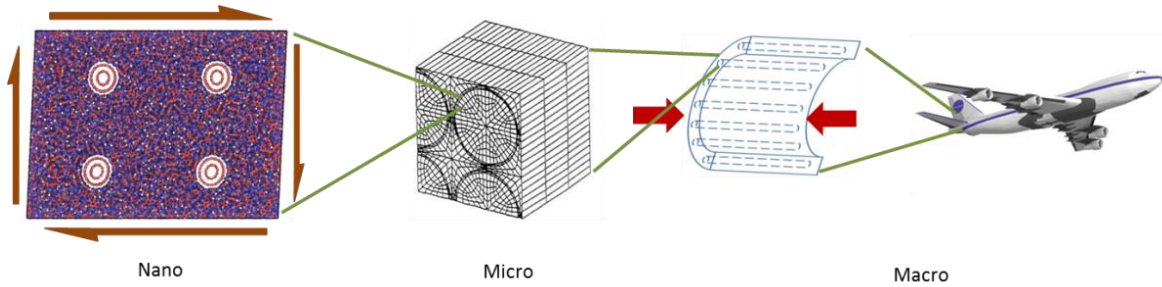


Figure 3.1: A Schematic Diagram Showing a Multiscale Approach to Calculate the Improvement in the Compressive Strength in MWNT Scrolled Fiber/Epoxy Composite

The first step was to run shear deformation on the MD model of the RVE using LAMMPS software under different strain rates. A parametric strain rate analysis was performed from the shear stress-strain data output from LAMMPS from different strain rates and a power law was relation was invoked to interpolate the shear modulus calculated from the nanoscale simulations. The shear modulus of the matrix was then used in the microscale Rule of Mixtures with 50% fiber volume fraction to calculate the shear modulus of the carbon fiber reinforced composite. The shear modulus of the composite was further used in the macroscale formula of modified Argon's formula to predict the compressive strength of the composite. The details of this methodology are explained in the following sections.

3.1.2 Macromechanics:

Earlier work by Rosen [10], which assumed extensional (transverse) and shear microbuckling of the fibers imbedded in an isotropic linearly elastic matrix, consistently over-predicted the compressive strength when compared with experimentally measured values. Argon [108] was among the first to recognize that fiber reinforced composites made by standard manufacturing processes, such as VARTM or even pultrusion, have regions of fiber misalignment.

Argon [108], and later Budiansky [28, 109], showed that fiber misalignments present in fiber reinforced composites could lead to yielding of the polymer matrix during deformation. The yielding of the matrix would, in turn, result in loss of matrix stiffness that could eventually trigger fiber microbuckling and resulting kink band formation leading to final failure [110]. Consequently, it was recognized that the dominant compressive failure mode in continuous fiber polymer matrix composites is localized compressive buckling, or kinking. Argon [108] proposed a simple yet elegant formula for composite strength given by

$$\sigma_c = \frac{\tau_Y}{\phi_o} \quad (3.1)$$

where, τ_Y is the matrix yield strength in shear, and ϕ_o is the initial fiber misalignment angle with respect to the load direction, sometimes referred to as fiber misorientation. Subsequently, a modified form of the Argon formula was derived that included both elastic and plastic buckling behavior as limiting cases [110-113],

$$\sigma_c = \frac{G_{12c}}{\left(1 + \frac{\phi_o}{\gamma_Y}\right)} \quad (3.2)$$

where, G_{12c} is the composite longitudinal shear modulus, τ_Y is the matrix yield strength in longitudinal shear, and γ_Y is the matrix yield strain in longitudinal shear.

The failure mechanism described in equation (3.2) is still a shear mode of fiber microbuckling, but unlike in Rosen's elastic analysis, it is the local nature of the imperfections, coupled with (perfectly) plastic yielding of the matrix in shear, that results in local microbuckling and kink band formation. From equation (3.2), it is apparent that improvements in the compressive strength of the composite could be achieved by: (a) improving the shear modulus of the matrix surrounding the fiber through the scrolling of MWNT sheets, and (b) by increasing the matrix yield strain in shear through the scrolling of MWNT sheets. However, the feasibility of this concept needs to be verified through Molecular Dynamics (MD) simulation of the effects of scrolled MWNT sheets that concurrently increases matrix yield strain and matrix shear modulus, thereby making use of synergies that may exist between these effects.

3.1.3 Micromechanics:

For continuous fiber-reinforced composites, the shear modulus can be calculated using the rule of mixtures [9] which relates to the dependence of the composite shear modulus on shear moduli of the constituent phases and their corresponding volume fractions. Based on the RVE schematic shown in Fig. 3.2 (a) and (b), before and after shear deformation respectively, the following formula for the composite shear modulus can be derived from micromechanics:

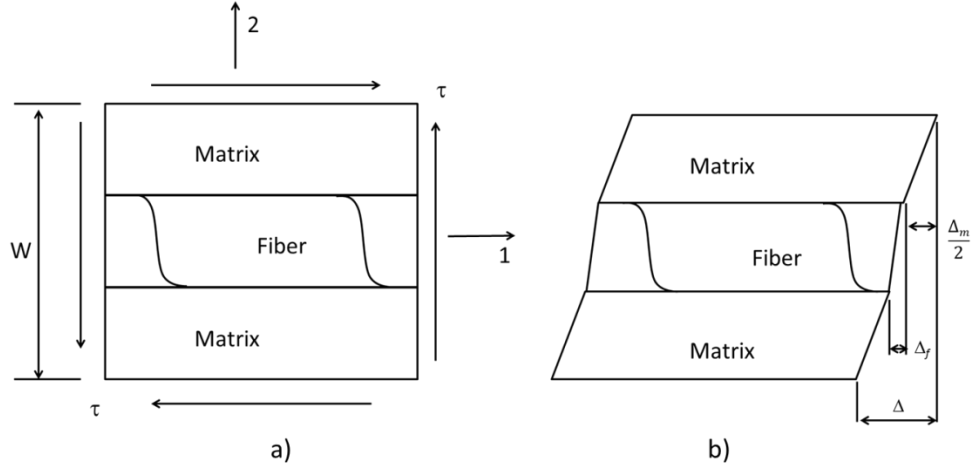


Figure 3.2: Representative Volume Element Loaded in Shear a) Shear Stress Loading b) Shear Deformation

$$G_{12c} = \frac{G_f G_m}{G_m V_f + G_f V_m} \quad (3.3)$$

where, G_{12c} is the longitudinal shear modulus of the composite, G_f is the shear modulus of the carbon fiber, G_m is the shear modulus of the matrix (with and without MWNT), and V_f and V_m are fiber volume ratio and the matrix volume fraction, respectively.

3.1.4 Nanoscale Simulations:

A schematic of the representative volume element (RVE) in the interface region of our MD model is depicted in Figure 3.3(a). The actual RVEs for baseline epoxy, one MWNT (0.94 vol%) embedded in epoxy, and four MWNTs (3.76 vol%) embedded in epoxy, used in computing compressive strength are depicted in Figures 3.4(a), (b) and (c), respectively. It should be noted that, unlike as shown in Figure 3.3 (a), the influence of the carbon fiber was not directly included in the nanoscale RVE due to length-scale issues, but was introduced through the micromechanical

model. After proper equilibration of the 3-D MD model, a uniform shear strain was imposed on the MD box at the operating temperature as depicted in Figure 3.3(a) together with periodic boundary conditions on the MD box. The shear stress vs. shear strain curve, as schematically depicted in Figure 3.3(b), was computed from the simulation for the scrolled interface region. Here, the goal was to use MD to obtain the matrix modulus (G_m) and the matrix shear strain at yield (γ_y) for the MWNT reinforced cases, and then use these computed material properties to obtain the compressive strength enhancement, if any, of the unidirectional carbon composite through the use of equations 3.3 and 3.2, respectively.

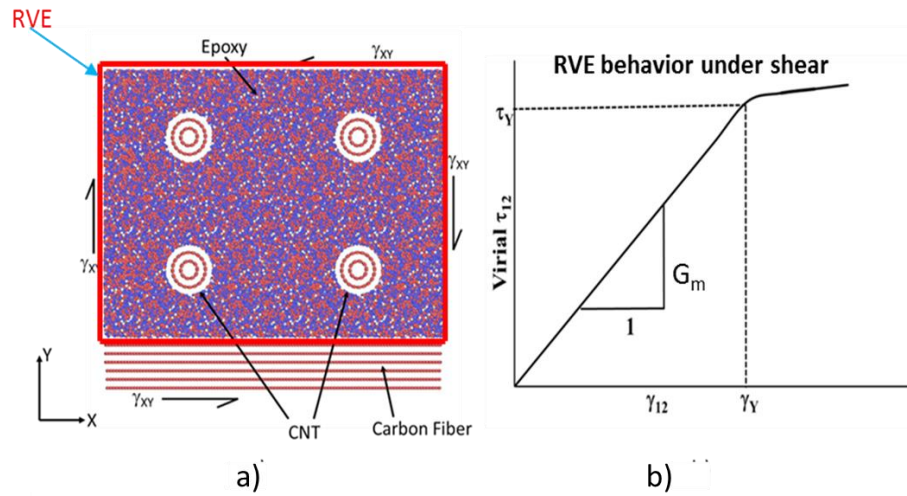


Figure 3.3: (a) MD Model of MWNT/EPON-862/Carbon Fiber Interface, (b) Virial Shear Stress versus Strain Curve Indicating Shear Modulus and Plastic Strain at Yield

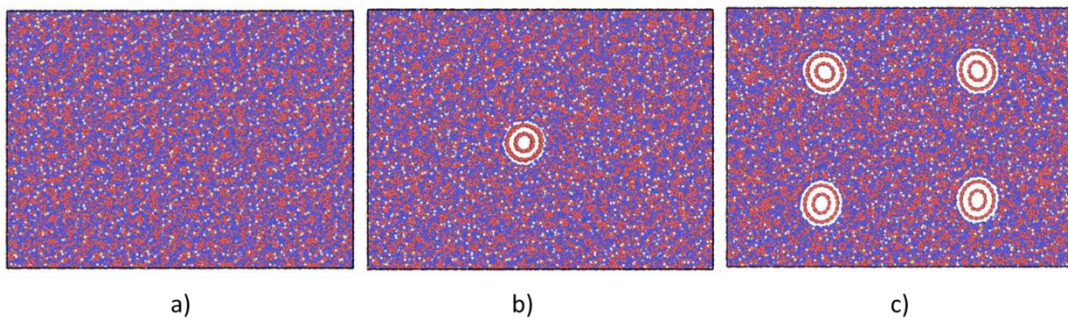


Figure 3.4: Molecular Model of (a) EPON-862 DETDA (Baseline) System, (b) EPON-862 DETDA with One MWNT Interface System, (c) EPON-862 DETDA with Four MWNTs Interface System

For the MD Simulations, the open-source LAMMPS software (developed by Sandia Labs) [105] was used. The stress tensor for any atom, I , is given by the following formula [114], where a and b take on values x, y, z to generate the 6 components of the symmetric tensor:

$$\tau_{ab} = - \left[\begin{aligned} & mv_a v_b + \frac{1}{2} \sum_{n=1}^{N_p} (r_{1a} F_{1b} + r_{2a} F_{2b}) + \frac{1}{2} \sum_{n=1}^{N_b} (r_{1a} F_{1b} + r_{2a} F_{2b}) + \\ & \frac{1}{3} \sum_{n=1}^{N_a} (r_{1a} F_{1b} + r_{2a} F_{2b} + r_{3a} F_{3b}) + \frac{1}{4} \sum_{n=1}^{N_d} (r_{1a} F_{1b} + r_{2a} F_{2b} + r_{3a} F_{3b} + r_{4a} F_{4b}) + \\ & \frac{1}{4} \sum_{n=1}^{N_i} (r_{1a} F_{1b} + r_{2a} F_{2b} + r_{3a} F_{3b} + r_{4a} F_{4b}) + Kspace(r_{ia}, F_{ib}) + \sum_{n=1}^{N_f} r_{ia} F_{ib} \end{aligned} \right] \quad (3.4)$$

The first term in equation (3.4) is a kinetic energy contribution for atom I . The second term is a pairwise energy contribution where n loops over the N_p neighbors of atom I , r_1 and r_2 are the positions of the 2 atoms in the pairwise interaction, and F_1 and F_2 are the forces on the 2 atoms resulting from the pairwise interaction. The third term is a bond contribution of similar form for the N_b bonds which atom I is part of. There are similar terms for the N_a angle, N_d dihedral, and N_i improper interactions that atom I is part of. There is also a term for the K_{Space} contribution from long-range Coulombic interactions. Finally, there is a term for the N_f fixes that apply internal constraint forces to atom I . Note that the virial stress for each atom is due to its interaction with all other atoms in the simulation, not just with other atoms in the group. These values of virial stresses for each atom in the system are used to compute the pressure of the entire system of atoms by LAMMPS. A symmetric pressure tensor is computed using the formula:

$$P_{IJ} = \frac{\sum_k^N m_k v_{k_I} v_{k_J}}{V} + \frac{\sum_k^N r_{k_I} f_{k_J}}{V} \quad (3.5)$$

Here, the first term uses components of the kinetic energy (temperature) and the second term uses components of the virial tensor that includes sum of pair, bonds, angles, dihedrals, improper, K_{space} and fixes contributions to the force on each atom, as discussed above. Because for this work we are concerned only with the Cauchy's stress induced by applied mechanical loads, thermal (residual) stresses were not included in the results.

3.1.5 Influence of Strain Rate:

A parametric sensitivity study on influence of the strain rate on compressive strength was performed where the MD models were subjected to shear deformation under different strain rates. It was observed that at different strain rates the models behaved differently. However, a common trend that was observed was that as the strain rate was reduced in the simulations, the shear modulus as well as the shear strain at yield was also reduced. The behavior of the pure epoxy baseline case, under different strain rates matched very well with the pattern followed by the experimental results by [113] on the same epoxy under different strain rates, albeit the experimental strain rates were much lower than the MD ones. Using these experimental data and the data from our MD simulations, a power law model was used to correlate the high strain rates of MD simulations to the lower experimental strain rates. A simple power law was devised to interpolate the entire interfacial shear stress vs shear strain curve as a function of shear strain rate and then calculate the shear modulus of the matrix as shown in Equation (3.6)-3.8.

$$G_m = A \left(\frac{\tau}{\gamma} \right)^n \quad (3.6)$$

where,

$$A = A_0 + A_1 \log \dot{\gamma}^* \quad (3.7)$$

$$n = n_0 + n_1 \log \dot{\gamma}^* \quad (3.8)$$

where, A_0 and A_1 are determined from the intercept values and n_0 and n_1 are determined from the slope values when plotted against the corresponding normalized strain rate, $\dot{\gamma}^*$. A normalized strain rate is defined in equation 3.9 where $\dot{\gamma}_{ref}$ is a reference strain rate selected as 0.01sec^{-1} :

$$\dot{\gamma}^* = \frac{\dot{\gamma}}{\dot{\gamma}_{ref}} \quad (3.9)$$

The power law coefficients A and n can be obtained by finding the logarithm of Eqn. (3.7 and 3.8) and then employing a linear regression analysis as depicted in Eqn. (3.10). The slope in Eqn. (3.10) provides the power law exponent n , and the intercept provides the power law coefficient A at a specified strain rate. The process needs to be repeated at different strain rates to obtain these parameters over the full strain-rate spectrum, as discussed in detail later in this dissertation.

$$\log \tau = \log A + n \log \gamma \quad (10)$$

3.2 COMPUTATIONAL MODELING DETAILS

The reactive force field, ReaxFF, was used for all the MD simulations described in this dissertation, using open source software, LAMMPS. The first step was to validate the MD model of the EPON 862 polymer. To do so, a strain rate effect study was performed by applying shear deformation on the MD model of the baseline epoxy at room temperature. The results from the shear stress versus strain data from the MD simulations were compared with the experimental data and the power law was used to determine the compressive strength of the Epoxy at the reference strain rate of 0.01 sec^{-1} . This compressive strength was used as the basis for the comparison on adding the MWNTs to the RVE of the epoxy system and to predict the enhancement.

The first system that was analyzed was baseline Epon 862-DETDA polymer, with an RVE of dimensions $13.5 \text{ nm} \times 10.3 \text{ nm} \times 6.8 \text{ nm}$ (Figure 3.5). For the purpose of this dissertation, this case of Baseline Epoxy MD model is called Case I. To apply the shear deformation on the molecular model of the epoxy, the following steps were incorporated for the modelling, temperature increase and equilibration:

1. First the epoxy model (courtesy of Michigan Tech), was minimized for about 10 picoseconds. This step allows the atoms to relax and achieve a state of minimum energy equilibrium before we could start increasing the temperature. Periodic boundary condition was maintained in the x , y and z directions.
2. Once the energy of this system was minimized, the temperature of the system was slowly increased at an increment of 30 K every 1 picosecond until it reached 300 K.
3. On reaching 300 K, the system was equilibrated at 300 K for about 10 picoseconds.

4. Uniform shear strain at different strain rates ranging from $2.43 \times 10^{13} \text{ sec}^{-1}$ to $2.43 \times 10^{11} \text{ sec}^{-1}$ was applied to the equilibrated system at 300 K.

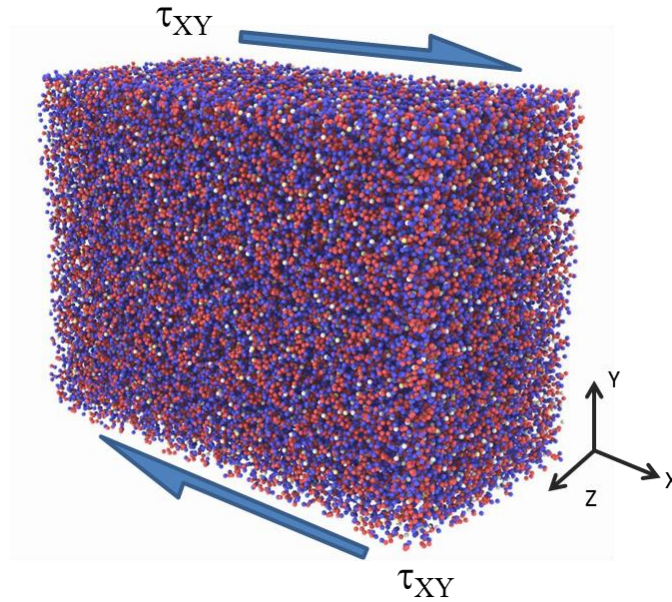


Figure 3.5: Case I – RVE Showing MD Model of Baseline Epoxy, EPON-862, Under Uniform Shear Deformation

The density of the baseline system was maintained at 1.19 g/cm^3 at 300 K for an atom count of 102,816 atoms. A maximum shear strain of about 11-25% was applied to the baseline system and the resulting shear stress was computed by LAMMPS using the virial stresses. An important point to note here is that, for the two models, periodic boundary conditions were maintained in all the three directions of x , y and z . The molecular images, as shown in Figure 3.3-3.5 were obtained using OVITO molecular graphics software [107]. For this dissertation, three different strain rates of $2.43 \times 10^{13} \text{ sec}^{-1}$, $2.43 \times 10^{12} \text{ sec}^{-1}$ and $2.43 \times 10^{11} \text{ sec}^{-1}$ were considered. The stress-strain values for these three cases of strain rates as computed by the MD simulations, were compared with the experimental results for the same epoxy system [113] at strain rates ranging from $1.3 \times 10^{-4} \text{ sec}^{-1}$

to 700 sec^{-1} . The shear stress vs. shear strain data from these MD simulations and the experimental results (as discussed in the Results section) were used to obtain the logarithmic plots for linear regression analysis. Finally, the variation of the power law parameters A and n as a function strain rate were obtained by fitting the data obtained from the logarithmic plots of stress vs strain. These data are in turn used in the power law (see equations 3.6-3.10) to calculate the shear modulus of the matrix from the shear stress at yield and strain from the MD results. Using these values in the Rule of Mixtures at a fiber volume fraction of 50% (Eqn. 3.3) the shear modulus of the composite was calculated. Further, using this value of the shear modulus of the whole composite in the modified Argon's formula (Eqn. 3.2) the compressive strength for the baseline epoxy with 50% fiber volume fraction was calculated under different strain rates and at a reference strain rate of 0.01 sec^{-1} . A nominal fiber misalignment angle of 0.1 radian was assumed in all calculations.

Once the baseline MD model was established, MWNTs were introduced to the baseline epoxy model. For this interface region between the epoxy and the MWNTs, the same RVE model of epoxy that was used to study the baseline case was used, with the dimensions of the epoxy as $13.5 \text{ nm} \times 10.3 \text{ nm} \times 6.8 \text{ nm}$. For studying the mechanical properties on introducing the MWNTs, two cases were studied, by introducing one and four MWNTs in the epoxy. This was done by displacing the atoms in the epoxy at a slow increment, until a cylindrical hole of the desired diameter including the van der Waal cut-off distance, was achieved. Two concentric carbon nanotubes were introduced in each of these holes within the epoxy, with chirality (5, 5) and (10, 10) with diameters 0.67 nm and 1.34 nm respectively, as shown in Fig. 3(b and c). The length of the MWNTs was 6.8 nm in the z -direction. Similar to the first case of pure baseline epoxy, periodic boundary conditions were maintained in all the three directions of x , y and z on introducing the MWNTs. In addition to enhancement in the mechanical properties of the CFRP

upon adding MWNTs to the system, a parametric sensitivity study was also conducted to study the influence of the wrapping angle of the scrolled MWNT sheet on the enhancement of the compressive strength, as depicted in Figure 3.6. It should be noted that the bias angle (α) represents the average orientation of the MWNT to the carbon fiber as not all MWNTs may be perfectly aligned along the length of the sheet,

For this, multiple cases were analyzed. The ones reported in this dissertation are as mentioned in Table 3.1:

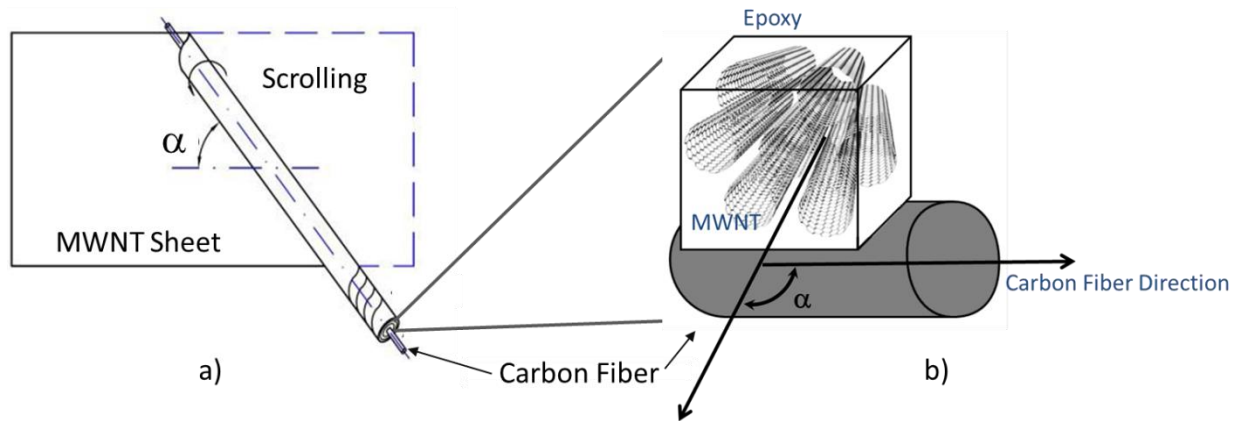


Figure 3.6: a) MWNT Sheet Scrolled on Carbon Fiber at a Bias Angle of α , b) Schematic of Nanoscale RVE of the Interface Region Between Epoxy-MWNT-Carbon Fiber with the Bias Angle α Between MWNT and Carbon Fiber

Table 3.1: Case Studies with Interpolation for Strain Rate Effect

Case I	Baseline epoxy model (discussed in the previous section)
Case II	Four MWNT/Epoxy Interface with shear deformation applied perpendicular to the length direction of the MWNTs (3.76 volume% of MWNTs)
Case III	Four MWNT/Epoxy Interface with shear deformation applied parallel to the length of the MWNTs (3.76 volume% of MWNTs)
Case IV	One MWNT/Epoxy Interface with shear deformation applied perpendicular to the length direction of the MWNTs (0.94 volume% of MWNTs.)
Case V	One MWNT/Epoxy Interface shear deformation applied parallel to the length of the MWNTs – (0.94 volume% of MWNTs)
Case VI	One MWNT/Epoxy Interface with shear deformation applied at 45° to the length direction of the MWNTs she(0.94 volume% of MWNTs)

A summary of the modelling, temperature equilibration and shearing procedure for these different cases are provided below:

Case II-V: Epoxy – with one and four MWNTs interface region

1. In this case, the first step is to minimize the Epoxy model for 10 picoseconds until it reaches its minimum energy state.
2. Then, the atoms in the region of the epoxy, where the MWNTs were to be placed, were slowly displaced, to create a cylindrical cavity (without deleting any atoms).
3. For Case with one MWNT, one cavity of about 2.1 nm diameters and throughout the z-axis length was created (while considering the van-der Waal’s distance between the atoms).

4. And for Cases with four MWNTs, four cavities of the same dimensions (as mentioned in the previous step) were created in the Epoxy model.
5. Then, the MWNTs were placed in these newly formed cavities, and the whole system of Epoxy-MWNTs was minimized again for 10 picoseconds.
5. The temperature of the system was raised to 300 K similarly as mentioned in Case I, by slowly increasing the temperature at an increment of 30 K every 1 picosecond until 300 K was reached.
6. On reaching 300 K, each system was equilibrated at 300 K for about 10 picoseconds.
7. Shear strain deformation of same strain rates that were used for the baseline case, i.e. from a range of $2.43 \times 10^{13} \text{ sec}^{-1}$ to $2.43 \times 10^{11} \text{ sec}^{-1}$ was applied to the equilibrated system at 300 K.

The density of these four cases, with one MWNT and with four MWNTs was maintained around 1.22 g/cm^3 and 1.32 g/cm^3 respectively at 300 K. The atom count on introducing one MWNT was increased to 104,436 and on introducing four MWNTs it was increased to 109,536 atoms. Again a maximum shear strain of about 11-25% was applied to all these cases and the resulting shear stress was computed by LAMMPS using the virial stresses. For cases II and IV, i.e., with 90° bias angle, the direction of the shear deformation was applied in a direction perpendicular to the length of the MWNT (Figure 3.7(a) and (c)). For computational simplicity and to avoid re-modeling the MD RVE, periodic boundary conditions of the MD model along the x, y and z directions was used for cases III and V, with 0° bias angle. For these cases, the shear direction on the MD system was changed from XY to YZ direction (Figure 3.7(b) and 3.7(d)) to apply the shear deformation along the length of the MWNT, i.e. shear deformation was applied parallel to the direction of the MWNTs.

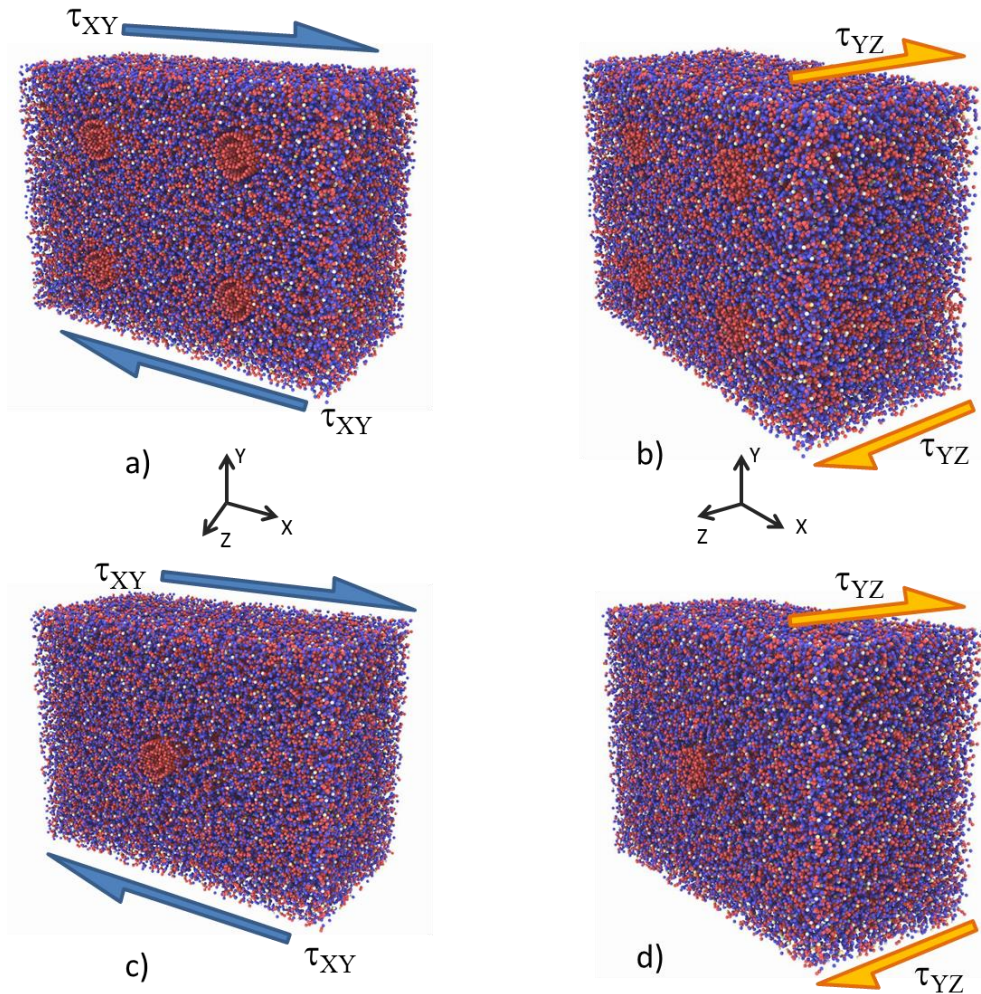


Figure 3.7: a) Case II – RVE showing Four MWNT/Epoxy Interface Shear Deformation Perpendicular to the Length of the MWNTs; b) Case III – RVE Showing Four MWNT/Epoxy Interface with Shear Deformation Along the Length of the MWNTs; c) Case IV – RVE Showing One MWNT/ Epoxy Interface 0° Shear Deformation Perpendicular to the Length of the MWNTs; d) Case V – RVE Showing One MWNT/Epoxy Interface with Shear Deformation Along the Length of the MWNTs

For Case VI, a different approach was used to apply the shear deformation at an angle of 45° to the longitudinal direction of MWNT in the RVE. In this case, the MWNT was placed in a cavity that was created at 45° to the X axis in the XZ plane and the shear deformation was applied in the XY direction. Figure 3.8 describes the RVE model. Figure 3.8 (a) shows the cross

section of the RVE, showing the embedded MWNT in the epoxy, and Figure 3.8 (b) is the top view of the Epoxy with MWNT at 45° to the XZ plane and the shear deformation in the XY plane. Similar to case IV and V, the density of this system was maintained at 1.22 g/cm^3 with 104,436 atoms count and a similar shear deformation as the previous cases, was applied in the XY direction. It was found after the MD simulation that for the 45° case, the CNT alignment changed slightly from 45° after the shear deformation, as discussed in the next chapter.

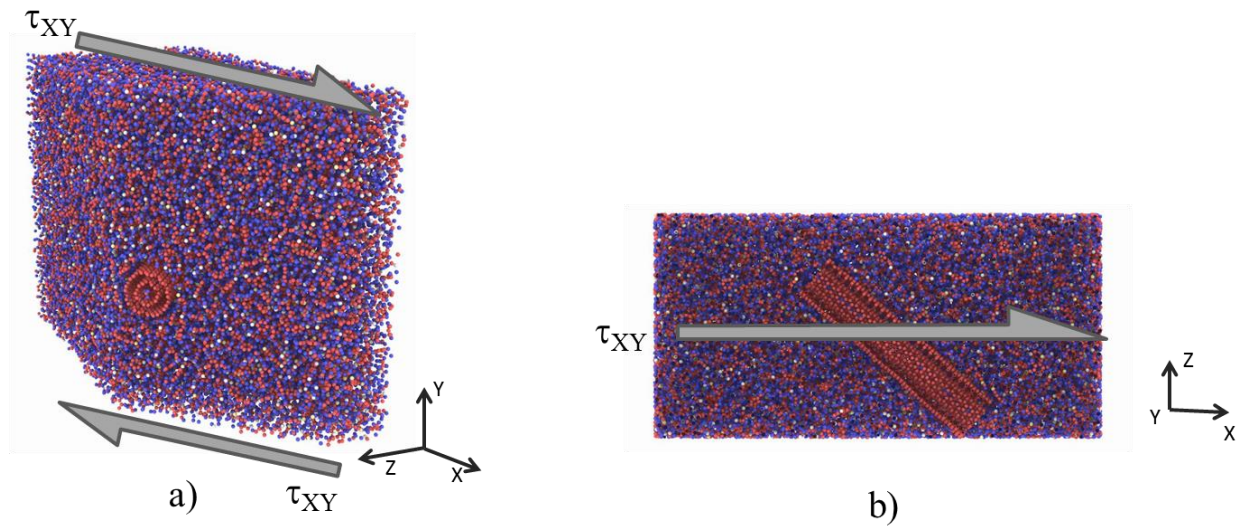


Figure 3.8: a) Case VI – RVE showing one MWNT/Epoxy Interface with MWNT Embedded at 45° to the XZ Plane. a) Cross-Sectional Image of Case VI; b) Top View of Case VI with the Shear Deformation Direction at 45° to the MWNT Longitudinal Direction (45° bias angle)

CHAPTER 4

RESULTS AND DISCUSSION

For the six different cases of RVEs under consideration, that is, baseline epoxy and epoxy with one and four MWNT in the interface region, and with shear deformation angles ranging from 0° , 45° and 90° , the systems were subjected to a maximum shear strain of 11-25% during the MD simulations at $T=300$ K. Periodic boundary conditions were used in all cases. Different strain rates were applied on these systems ranging from 10^{13} to 10^{10} sec^{-1} , and it was observed that as the applied strain rate was decreased, the maximum shear strength at yield decreased significantly, as did the shear modulus. Figure 4.1 shows a study of shear stress vs shear strain at different strain rates for the baseline RVE obtained from our MD simulations and from published experimental data [113]. Based on this study a strain rate of 2.43×10^{11} sec^{-1} , which is deemed low by MD standards, was selected as the reference strain rate for further analysis of the other RVEs as described later.

It is important to note that typical MD-based predictions of the mechanical properties of epoxy models ignore the influence of the simulated strain rates. For a wide range of strain rates the shear modulus of Epon-862 are on the same order, and since the experimental strain rates are virtually impossible to achieve for fully atomistic models due to time-scaling issues, it was necessary to develop a linear regression model. Therefore, a simple power law was devised as discussed in 3.1.5 to interpolate the shear modulus calculated from the MD results, as a function of the shear strain rate.

4.1 Baseline Epoxy Model (Case I) With Interpolation For Strain Rate Effect

The first part of this dissertation involved verifying the compressive strength of the baseline carbon fiber reinforced polymer composite from the MD simulations with that of the experimental results available in the literature. To do this, shear stress deformation was applied on a nanoscale MD model of baseline epoxy at different strain rates ranging from 10^{11} sec^{-1} to 10^{13} sec^{-1} (Figure 4.1). These results were then used in the power law followed by the microscale and finally the macroscale formula as described in the previous chapter.

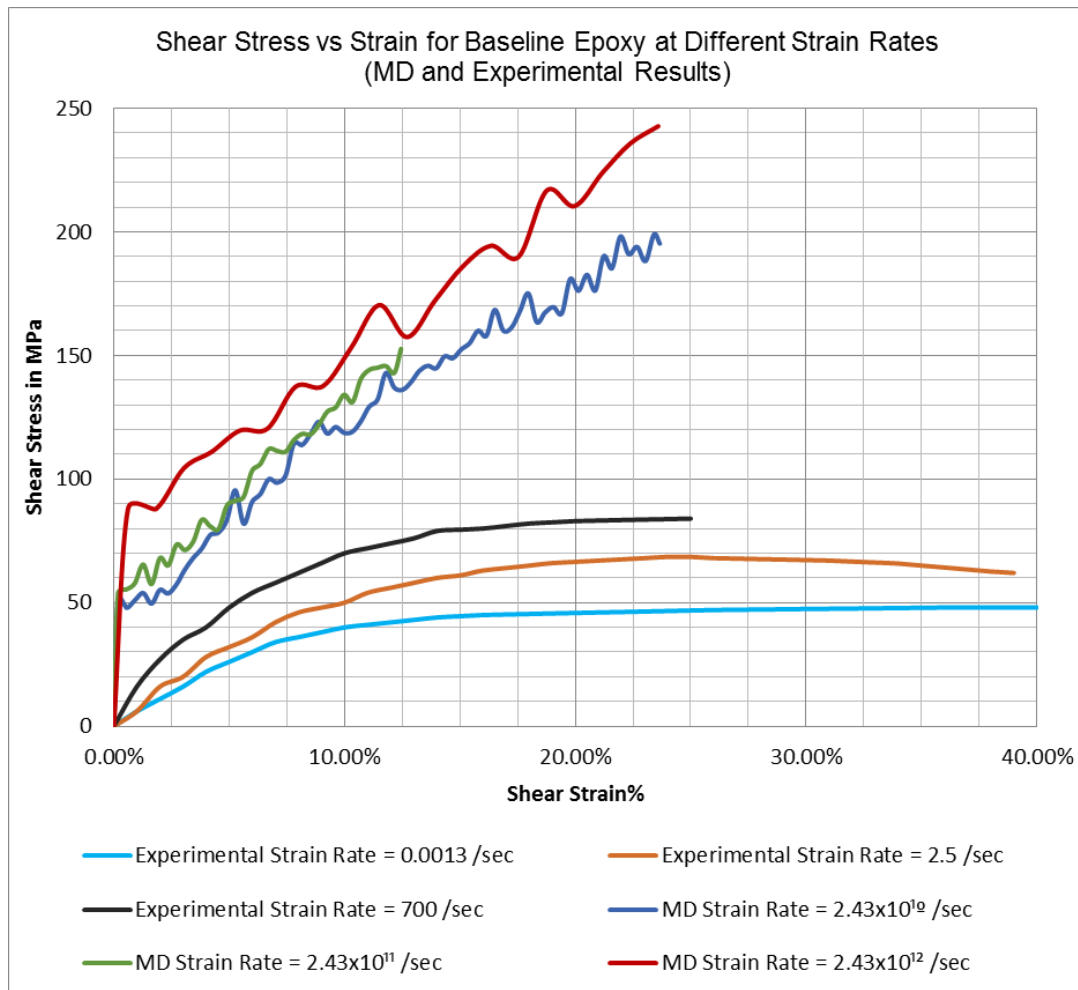


Figure 4.1: Shear Stress vs Strain at Different Strain Rates for Epon-862 at 300 K

These shear stress vs strain plots from MD and experimental results were then plotted in a logarithmic shear stress vs logarithmic strain plots as shown in Figure 4.2. From this log-log plot, the intercept (A_i) and the slope (n_i) of the regression values for each strain rate was obtained and plotted against the corresponding normalized strain rate ($\dot{\gamma}^*$) as shown in Figure 4.3(a) and (b) respectively. The formula used to compute normalized strain rate was as discussed in section

3.1.5, Equation 3.8, given by
$$\dot{\gamma}^* = \frac{\dot{\gamma}}{\dot{\gamma}_{ref}}$$

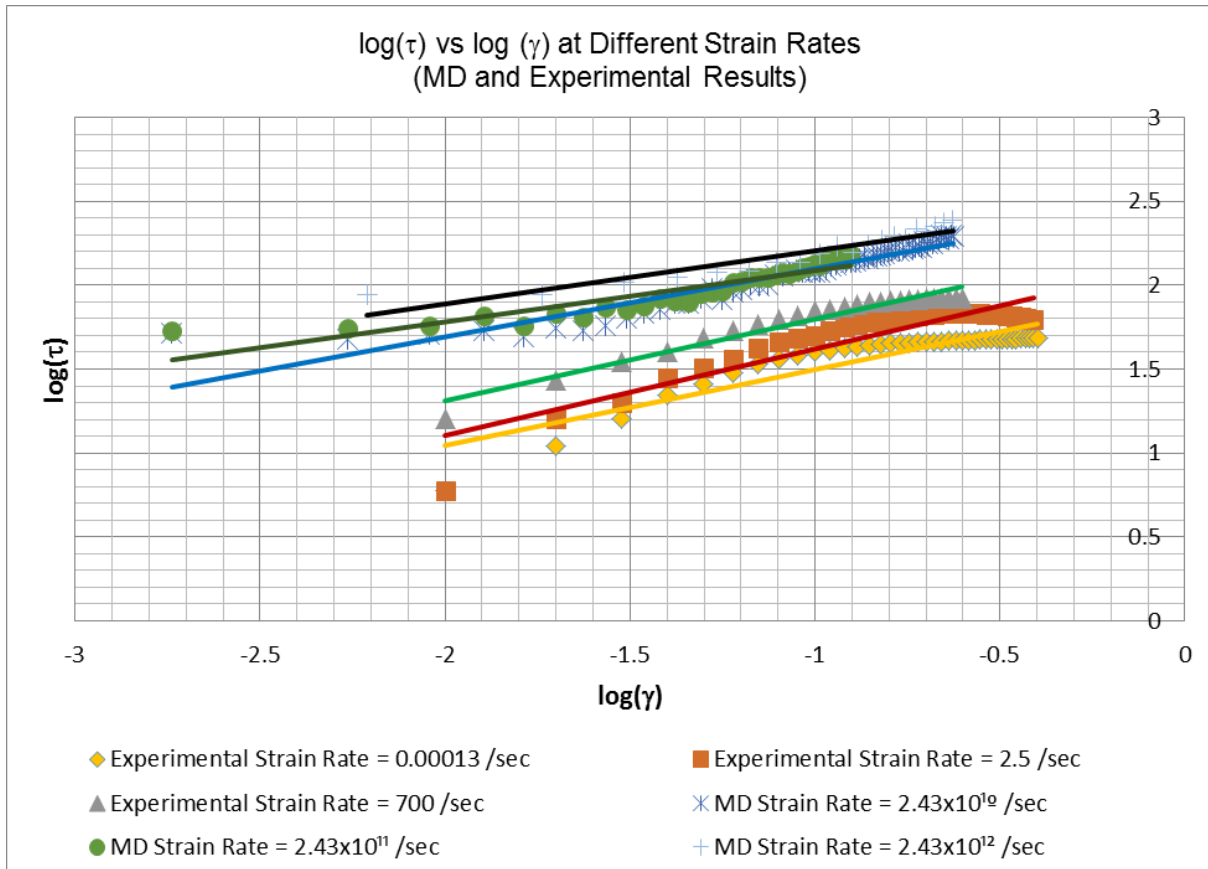


Figure 4.2: Log Shear Stress vs Log Strain for Epon-862 at 300 K under Different Strain Rates

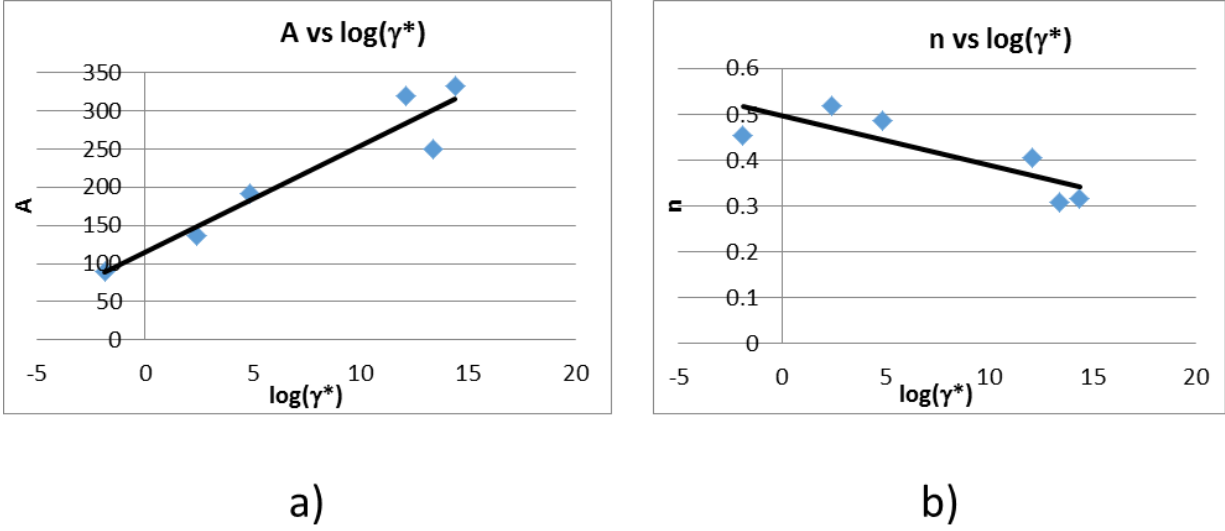


Figure 4.3: (a) Variation of the Power Law Intercept A , and (b) Power Law Exponent n for Epon-862 Matrix at 300 K for with their Corresponding Normalized Strain Rates

The slope (A_1) and intercept (A_0) from Fig. 4.3 (a) was used to determine the power law coefficients A as a function of strain rate using the following formula: $A = A_0 + A_1 \log \dot{\gamma}^*$. Similarly, the slope (n_1) and intercept (n_0) from Fig. 4.3 (b) was used to determine the power law exponent n as a function of strain rate using the following formula: $n = n_0 + n_1 \log \dot{\gamma}^*$. Once A and n were obtained from through fitting simulation and test data, these values were further used to calculate the shear modulus of the matrix (G_m) at any given strain rate, using the power law $G_m = A \left(\frac{\tau}{\gamma} \right)^n$, where the shear stress at yield, τ and yield strain, γ are output from the MD simulation as discussed in Chapter 3.

Once the shear modulus of the matrix was determined from MD computations, we used this value of G_m in the microscale formula, the Rule of Mixtures (Eqn 3.3): $G_{12c} = \frac{G_f G_m}{G_m V_f + G_f V_m}$. At a fiber volume fraction of 50% and using the shear modulus of carbon fiber as 5 GPa [115], we determine the shear modulus of the composite and eventually compressive strength of the

composite using the modified Argon's formula (Eqn. 3.2) : $\sigma_c = \frac{G_{12c}}{\left(1 + \frac{\phi_o}{\gamma_Y}\right)}$, at a reference strain

rate of 0.01 sec^{-1} . The tabulated results for the power law coefficients, yield strain and shear stress at yield (from MD data, shear modulus of the matrix (Power Law), shear modulus of the composite (from Rule of Mixtures), and the compressive strength of the composite (Modified Argon's formula), for baseline carbon fiber reinforced composite are as shown in Table 4.1.

From these data, the compressive strength of baseline unidirectional carbon/epoxy composite at the reference strain rate of 0.01 sec^{-1} was predicted to be 665 MPa, which is in reasonably good agreement with the experimentally observed range of 550-800 MPa for this material system [9], assuming a nominal 50% fiber volume fraction .

Table 4.1: Compressive Strength of Baseline CFRP from MD Simulations at Different Strain Rates

	2.43×10^{12} /sec	2.43×10^{11} /sec	2.43×10^{10} /sec	0.01 /sec
A=	316	302	284	115
n=	0.3407	0.3515	0.3656	0.4961
$\gamma_Y =$	0.0182	0.0127	0.0127	0.0124
$\tau_Y =$	88 MPa	65.4 MPa	53.8 MPa	57.8 MPa
$G_m =$	5680 MPa	6091 MPa	6012 MPa	7597 MPa
$G_f =$	5000 MPa	5000 MPa	5000 MPa	5000 MPa
$V_f =$	0.5	0.5	0.5	0.5
$G_{12c} =$	5318 MPa	5492 MPa	5460 MPa	6030 MPa
$\phi_o =$	0.1	0.1	0.1	0.1
$\sigma_c =$	821 MPa	619 MPa	616 MPa	665 MPa

4.2 Modeling Epoxy Embedded with One and Four MWNTs (Case II and IV) With Interpolation for Strain Rate Effect

After establishing and verifying the MD model for the baseline epoxy, MWNTs were introduced in the epoxy system as discussed in Section 3.2 and shear deformation simulations were performed for cases II-VI. On applying shear deformation to the RVE of Epon-862 perpendicular to the length of the MWNTs with one MWNT (0.94 vol%) and four MWNTs (3.76 vol%), (cases II and IV) respectively, at different strain rates, a similar trend as that of baseline epoxy case was observed, where the yield strength on the shear stress versus shear strain curve decreased with decreasing strain rate. This trend was observed for both Case II and IV and is shown in Figure 4.4 and 4.5, respectively. Comparing computed shear stress vs. shear strain data for baseline epoxy (Case I) , Case II (one MWNT) and Case IV (four MWNT) at a strain rate of $2.43 \times 10^{11} \text{ sec}^{-1}$ shows significant increase in the slope as well as yield strength of the shear stress versus strain plots as compared with the baseline model (Figure 4.6).

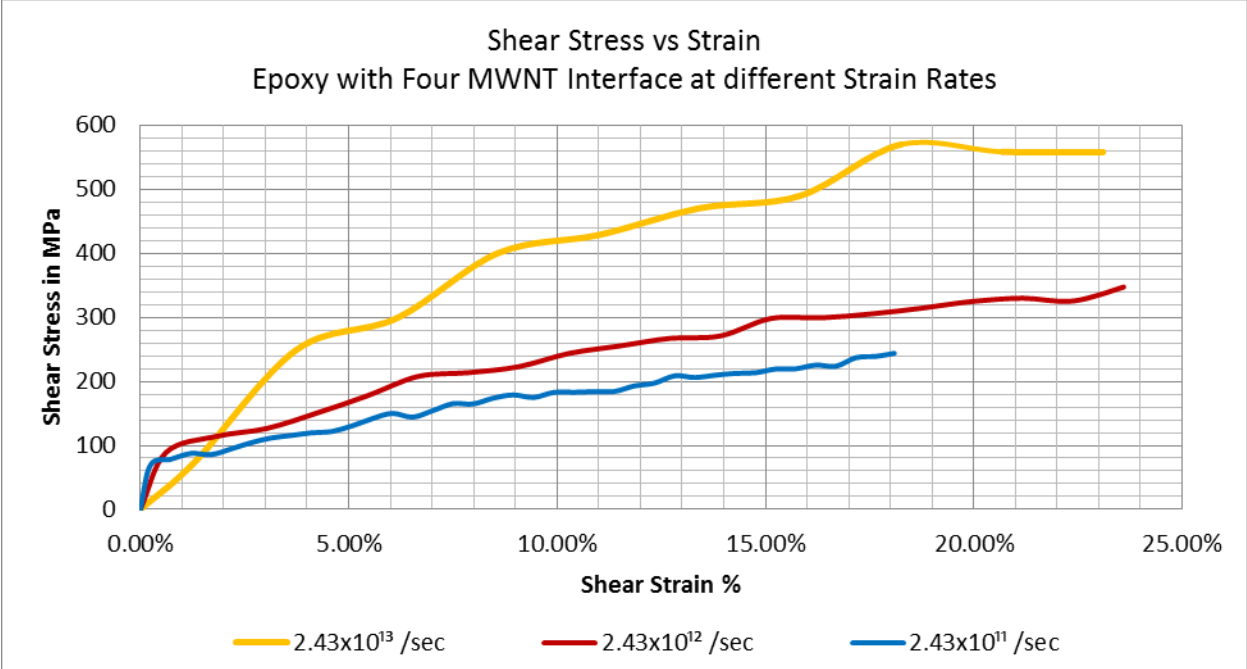


Figure 4.4: Shear Stress Vs Strain Comparison for Case II RVE - Epoxy With Four MWNT, at Different Strain Rates at 300K

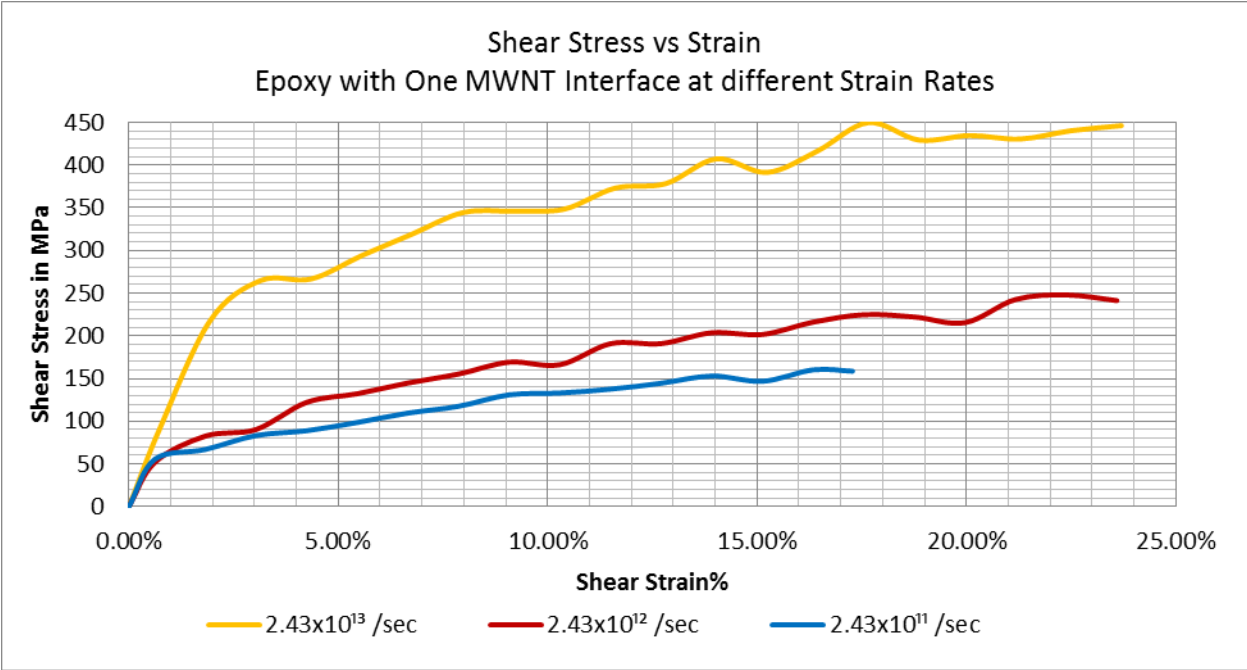


Figure 4.5: Shear Stress Vs Strain Comparison for Case IV RVE - Epoxy With One MWNT, at Different Strain Rates at 300K

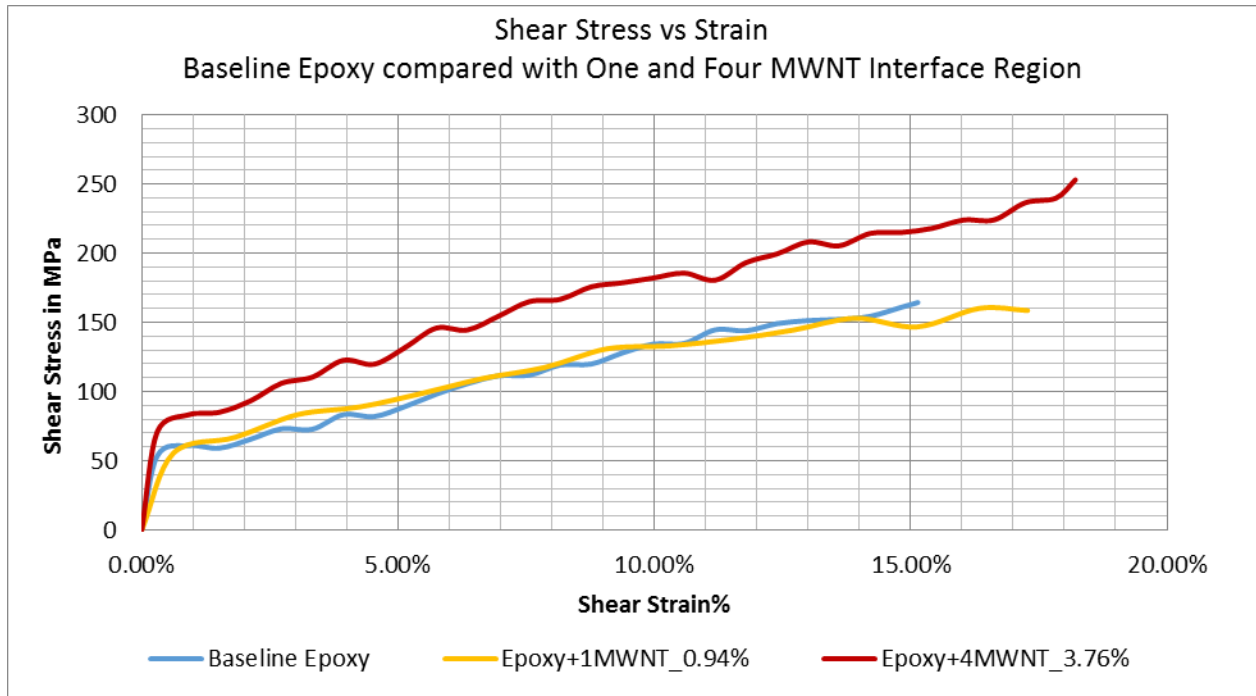


Figure 4.6: Shear Stress Vs Strain Comparison Between Baseline Epoxy, Epoxy With One MWNT and Epoxy With Four MWNT at a Strain Rate of 2.43×10^{11} /sec at 300K

Since the added MWNT volume fraction is very low compared to the epoxy volume fraction, it was assumed that the trend of decreasing slope of the shear stress-strain curve (i.e., shear modulus) at lower strain rates is primarily governed by the epoxy system and was independent of the vol% of MWNTs. Hence, the same values of the power law coefficients, A and n that were calculated for the baseline epoxy case, were used to determine the shear modulus of the matrix RVE with one and four MWNTs. The shear modulus and the compressive strength of the composite with 0.94 vol% and 3.76 vol% MWNT were computed using the multiscale modeling procedure as mentioned earlier for baseline epoxy. The enhancement in the shear modulus and the compressive strength, for shear deformation applied perpendicular to the MWNT length axis, at the reference strain rate of 0.01 sec^{-1} are tabulated below in Table 4.2 together with all of the parameters used in the multiscale model:

Table 4.2: Compressive Strength Enhancement Comparison on Adding One and Four MWNTs, from MD Simulations, at the Reference Strain Rate of 0.01 /Sec for Shear Deformation Applied Perpendicular to the MWNT Axis at a Strain Rate of 0.01 /sec

	Baseline CFRP Case I	CFRP reinforced with Four MWNTs (3.76 vol%) Case II	CFRP reinforced with One MWNT (0.94 vol%) Case IV
A=	115	115	115
n=	0.4961	0.496	0.4961
$\gamma_Y =$	0.0124	0.021	0.015
$\tau_Y =$	57.8 MPa	86 MPa	72 MPa
$G_m =$	7597 MPa	7875 MPa	7708 MPa
$G_f =$	5000 MPa	5000 MPa	5000 MPa
$V_f =$	0.5	0.5	0.5
$G_{12c} =$	6030 MPa	6116 MPa	6066
$\phi_o =$	0.1	0.1	0.1
$\sigma_c =$	665 MPa	893 MPa	791 MPa
%Improvement over Baseline Epoxy	-	34.3%	19%

From Table 4.2 it can be observed that there is a 34% improvement in predicted compressive strength over baseline epoxy when the carbon fiber is overwrapped with MWNT perpendicular to the fiber direction for a MWNT vol% of 3.76, and a 19% improvement when the carbon fiber is overwrapped with MWNT perpendicular to the fiber direction for a MWNT vol% of 0.94.

4.3 Study of the influence of Overwrap Angle of MWNT sheet on carbon fiber With Interpolation for Strain Rate Effect

The next step was to study the influence of intermediate overwrap angle of the MWNTs on the carbon fiber, besides 90° overwrap angles as already reported earlier in this chapter. For this purpose, a 0° and 45° overwrap angle case was studied for one MWNT embedded in the epoxy, i.e., Case V and Case VI, as shown in Figure 3.7 (d) and 3.8. Strain rates ranging from $2.43 \times 10^{11} \text{ sec}^{-1}$ to $2.43 \times 10^{13} \text{ sec}^{-1}$ were applied to these case and similar strain rate dependency was observed for both Case V and VI as the baseline case. Similar to the methodology used in cases, I, II and IV, a multiscale method of calculating the compressive strength of the composite was employed for Cases V and VI. It was observed that on applying the shear deformation, for case VI, the MWNT alignment had changed from the initial 45° to 47° at the end of shear deformation simulation under a strain rate of $2.43 \times 10^{11} \text{ sec}^{-1}$. First the shear modulus from the MD simulation was calculated using the same power law coefficients derived from the baseline simulations and strain rate analysis. This was followed by the application of the rule of mixtures to calculate the shear modulus of the carbon composite with a fiber volume fraction of 50%, and finally modified Argon's formula was to predict the compressive strength of the unidirectional composite at the macroscale. Table 4.3 summarizes and compares the results from these calculations for Cases III, IV and VI at a strain rate of 0.01 sec^{-1} with the baseline CFRP case. Figure 4.7 compares the shear stress versus strain plots for the baseline epoxy RVE model with one MWNT embedded (i.e., 0.94 vol%) in the epoxy with MWNT oriented at 0°, 45° and 90° bias angles to the carbon fiber longitudinal direction, respectively. From Table 4.3 it can be observed that the composite compressive strength is fairly sensitive to the MWNT angle with the

carbon fiber longitudinal direction and that the maximum improvement in predicted compressive strength over baseline epoxy occurs when the carbon fiber is overwrapped with MWNT perpendicular to the fiber direction for 0.94 vol% of MWNT.

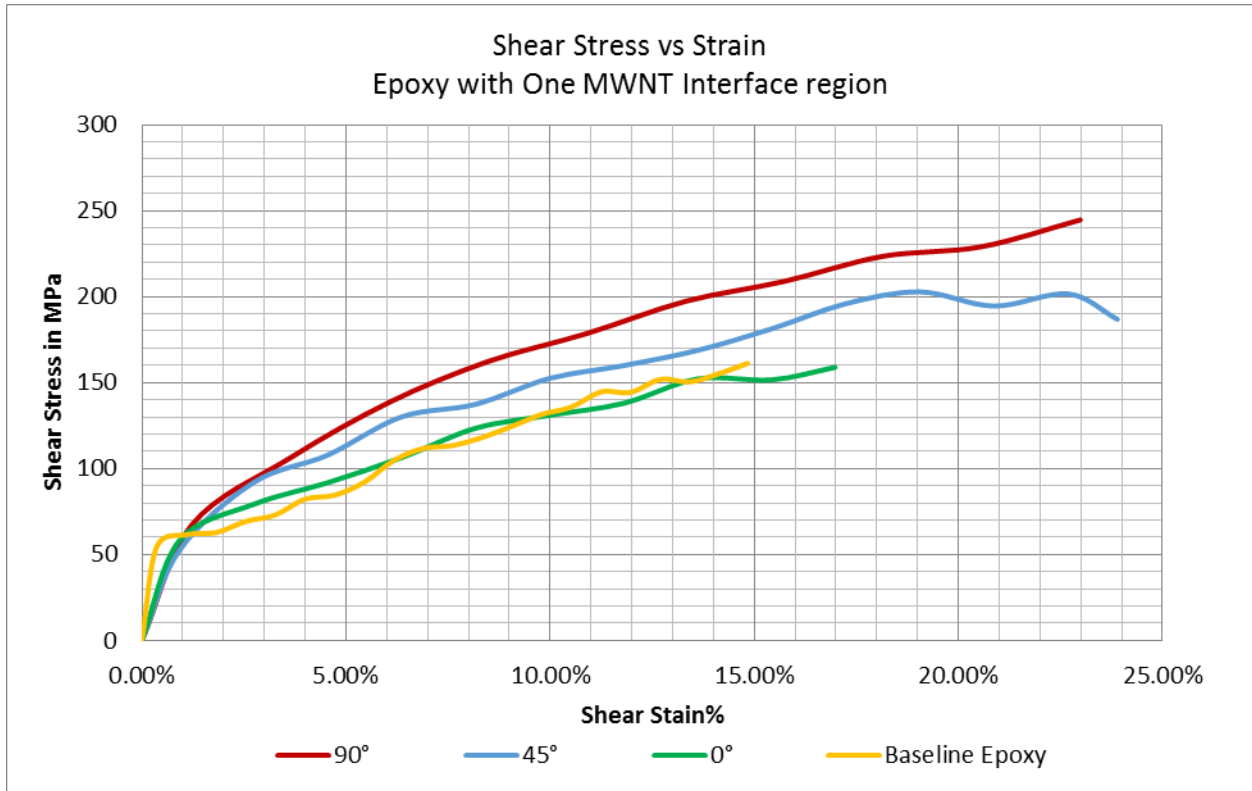


Figure 4.7: Shear Stress vs Strain comparison between Baseline Epoxy, Epoxy with One MWNT under shear deformations at angles 0°, 45° and 90° at a strain rate of 2.43×10^{11} /sec at 300 K

Table 4.3: Compressive Strength Enhancement Comparison On Adding One MWNT At 0°, 45° And 90° Bias Angle, at The Reference Strain Rate of 0.01 /sec

	Baseline CFRP Case I	CFRP reinforced with One MWNT At 0° deformation angle (0.94 vol%) Case III	CFRP reinforced with One MWNT At 45° deformation angle (0.94 vol%) Case VI	CFRP reinforced with One MWNT At 90° deformation angle (0.94 vol%) Case IV
A=	115	115	115	115
n=	0.4961	0.4961	0.4961	0.4961
$\gamma_Y =$	0.0124	0.013	0.0135	0.015
$\tau_Y =$	57.8 MPa	62 MPa	65 MPa	72 MPa
$G_m =$	7597 MPa	7684 MPa	7720 MPa	7708 MPa
$G_f =$	5000 MPa	5000 MPa	5000 MPa	5000 MPa
$V_f =$	0.5	0.5	0.5	0.5
$G_{12c} =$	6030 MPa	6058 MPa	6069 MPa	6066
$\phi_o =$	0.1	0.1	0.1	0.1
$\sigma_c =$	665 MPa	697 MPa	722 MPa	791 MPa
%Improvement over Baseline	-	4.7%	8.5%	19%

From Table 4.2 and 4.3 it was established that on adding MWNTs to the interface region of epoxy-carbon fiber, an improvement in the compressive strength of the composite up to 19% with volume fraction of 0.94 % and increasing the volume fraction to 3.76% results in an improvement of as 34%. Next, the influence of overwrap angle at higher MWNT volume fraction of 3.76% was studied. Figure 4.8 shows the improvement in the shear stress versus strain slope over baseline epoxy case, when four MWNTs were embedded in the epoxy and shear deformation was applied at 0° and 90° angles to the RVE. Because of the complexity of MD modeling, only two cases, 0° and 90° bias angles were studied for the 3.76 volume % of

MWNTs. Table 4.4 summarizes the predicted enhancement and the influence of the overwrap angle on the compressive strength of the CFRP when wrapped with a MWNT volume fraction of 3.76%.

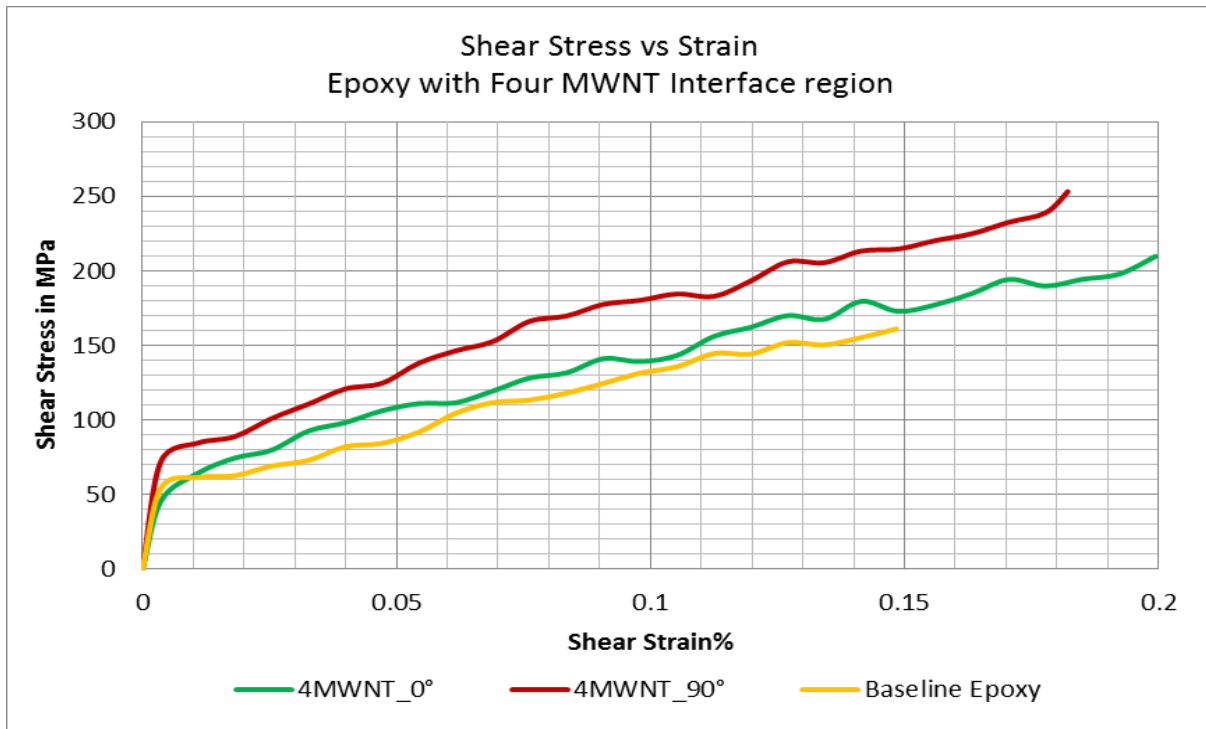


Figure 4.8: Shear Stress Vs Strain Comparison between Baseline Epoxy, Epoxy with Four MWNT under Shear Deformations at angles 0° and 90° at a Strain Rate Of 2.43×10^{11} /sec at 300 K

Table 4.4: Compressive Strength Enhancement Comparison On Adding Four MWNT At 0°, And 90° Shear Deformation Angles, At The Reference Strain Rate Of 0.01 /sec At 300K

	Baseline CFRP <u>Case I</u>	CFRP reinforced with Four MWNT At 90° deformation angle (3.76 vol%) <u>Case II</u>	CFRP reinforced with Four MWNT At 0° deformation angle (3.76 vol%) <u>Case III</u>
A=	115	115	115
n=	0.4961	0.496	0.4961
$\gamma_Y =$	0.0124	0.021	0.0144
$\tau_Y =$	57.8 MPa	86 MPa	69 MPa
$G_m =$	7581 MPa	7875 MPa	7701 MPa
$G_f =$	5000 MPa	5000 MPa	5000 MPa
$V_f =$	0.5	0.5	0.5
$G_{12c} =$	6026 MPa	6116 MPa	6063 MPa
$\phi_o =$	0.1	0.1	0.1
$\sigma_c =$	665 MPa	893 MPa	763 MPa
%Improvement over Baseline	-	34.3%	14%

From Tables 4.3 and 4.4, it is evident that the shear modulus of the matrix and hence the compressive strength of the composite for cases with MWNT oriented perpendicular to the carbon fiber is higher than the 45° and 0° bias angle cases, independent of MWNT volume fraction. Comparing the shear modulus of the four MWNTs embedded in the epoxy matrix (G_m), calculated from the power law (at a strain rate of 0.01 sec⁻¹), an improvement of 2.6% was observed with 90° overwrap bias angle over the 0° overwrap bias angle case (Table 4.6). To analytically verify this observation from MD simulations, a semi empirical formula based on the Halpin-Tsai method was used [116] to calculate the shear modulus of Epon-862 polymer matrix with reinforced MWNTs. The dimensions of the RVE in consideration for the Halpin-Tsai

method calculations were used exactly identical to the RVE used in the MD simulations. To calculate the shear modulus of the matrix with four embedded MWNTs, for the two cases, i.e. 0° and 90° overwrap bias angles, the following Halpin-Tsai formulas were used:

$$G_{12} = \frac{G_m (1 + \xi \eta V_{MWNT})}{(1 - \eta V_{MWNT})} \quad (4.1)$$

$$G_{23} = \frac{E_2}{2(1 + \nu_{23})} \quad (4.2)$$

Where G_{12} is the shear modulus calculated for the RVE where shear deformation direction is at 0° angle to the direction of the MWNTs and G_{23} is the shear modulus calculated for the same RVE but with transverse shear loading direction, i.e., shear loading direction is 90° to the MWNTs. The other variables are calculated using the following formulas:

$$\xi = 1 + (40 V_{MWNT}^{10})$$

$$\eta = \frac{\left(\frac{G_{MWNT}}{G_m} - 1 \right)}{\left(\frac{G_{MWNT}}{G_m} + \xi \right)}$$

$$\nu_{23} = \nu_{13} \frac{E_2}{E_1}$$

$$\nu_{13} = \nu_{MWNT} V_{MNWNT} + \nu_m V_m \quad (4.3)$$

$$E_1 = (E_m V_m) + (E_{MWNT} V_{MWNT})$$

$$E_2 = \frac{E_m E_{MWNT}}{(V_m E_{MWNT}) + (V_{MWNT} E_m)}$$

here, E_m and E_{MWNT} are the Young's modulus of the polymer matrix and the MWNT respectively; G_m and G_{MWNT} are the Shear Modulus; ν_m and ν_{MWNT} are the Poisson's ratio of the polymer matrix and MWNT respectively [113] V_m is the matrix volume fraction and V_{MWNT} is the MWNT volume fraction (Table 4.5).

As can be observed from Table 4.6, both Halpin –Tsai and strain-rate interpolated MD models predict that the 90° bias angle shows the highest enhancement in shear modulus of the epoxy matrix in the presence of imbedded MWNTs at volume fraction of 3.76%. However, the Halpin-Tsai analytical model predicts a much larger (23%) improvement in the shear modulus of the matrix with MWNT at 90° bias angle, whereas the MD model predicts only an increase of 3%. The discrepancy is likely due to the fact that Halpin-Tsai model is a two-dimensional

micromechanical model which does not account for the non-bonded interactions between the MWNT and the epoxy matrix.

Table 4.5: EPON-862 and MWNT Properties for Halpin-Tsai Calculations under Quasi-Static Loading

	<u>Epoxy</u> ^[117]	<u>MWNT</u> ^[118]
Volume Fraction	0.9624 (V_m)	0.0376 (V_{MWNT})
Young's Modulus (GPa)	2.56 (E_m)	1050 (E_{MWNT})
Shear Modulus (GPa)	0.946 (G_m)	500 (G_{MWNT})
Poisson's Ratio	0.353 (ν_m)	0.27 (ν_{MWNT})

Table 4.6: Comparison of Halpin-Tsai Calculations with MD Simulation Results for A Strain Rate Of 0.01/sec

	\underline{G}_{12} (Shear Deformation at 0° angle to the <u>MWNT</u>)	\underline{G}_{23} (Shear Deformation at 90° angle to the <u>MWNT</u>)	<u>% Improvement</u>
Halpin-Tsai Calculations	1.077 GPa	1.32 GPa	22.6%
MD Simulations (for Four MWNTs embedded in EPON-862 polymer)	7.7 GPa	7.9GPa	2.6%

4.4 Experimental Verification

In this section, verification of the multiscale model is carried out by comparing the MD results with (a) experimental data from nanoindentation tests performed at UT-Dallas, and (b) experimental results from three-point bending tests on MWNT wrapped carbon-fiber/epoxy composite beams.

(a) Nanoindentation Tests

Nanoindentation tests were performed at UT-Dallas on a single carbon fiber wrapped with CNT sheet and embedded in epoxy matrix. Compressive modulus for the composite with the wrapped CNT sheet (at 0° and 45° bias angle) at different regions of the specimen were obtained using this method as shown in Figure 4.9 and as tabulated in Table 4.7. Oliver-Pharr equation [119] was used to predict the modulus of the composite in the longitudinal direction from the nanoindentation tests.

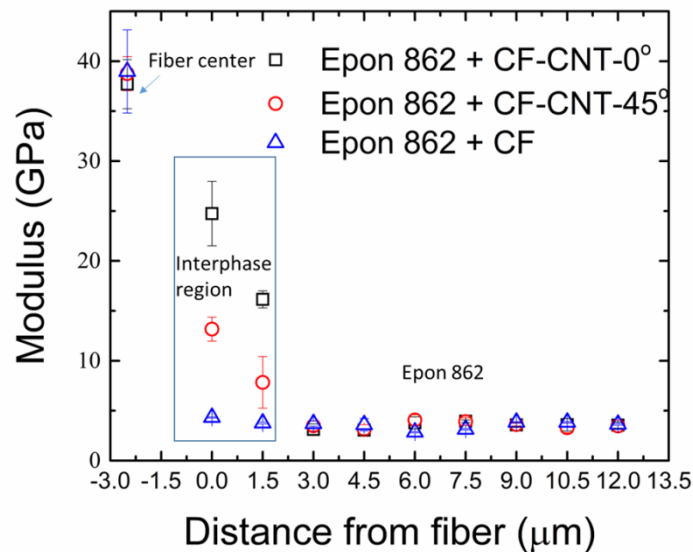


Figure 4.9: Modulus Estimation from Nanoindentation Tests (Courtesy: University Of Texas-Dallas)

Table 4.7: Modulus from Nanoindentation Tests

Modulus (GPa)	<u>Carbon fiber with wrapped CNT sheet at 0° bias angle embedded in epoxy</u>	<u>Carbon fiber with wrapped CNT sheet at 90° bias angle embedded in epoxy</u>	<u>Baseline</u>
Interphase near to fiber	24.7±3.2	13.2±1.2	4.33±0.05
Interphase near to Epoxy	16.1±0.9	7.8±2.6	3.76±0.08

To compare the compressive modulus from the nanoindentation tests with the MD results, compressive simulations were performed on the nanoscale epoxy-MWNT interface region with two different MWNT volume fractions (0.94% and 3.76%). Comparing computed compressive stress vs. strain data for the two cases of volume fraction at a strain rate of $1.0 \times 10^{10} \text{ sec}^{-1}$ show significant increase in the slope of the stress versus strain plots when the volume fraction of MWNT is increased from 0.94% to 3.76% as shown in Figure 4.10. Using the stress-strain data from different strain rates and applying the power law approach discussed in Chapter 4, the modulus of the epoxy-MWNT interface region was calculated as summarized in Table 4.8 for the actual nanoindentation strain rate of 0.001 /sec.

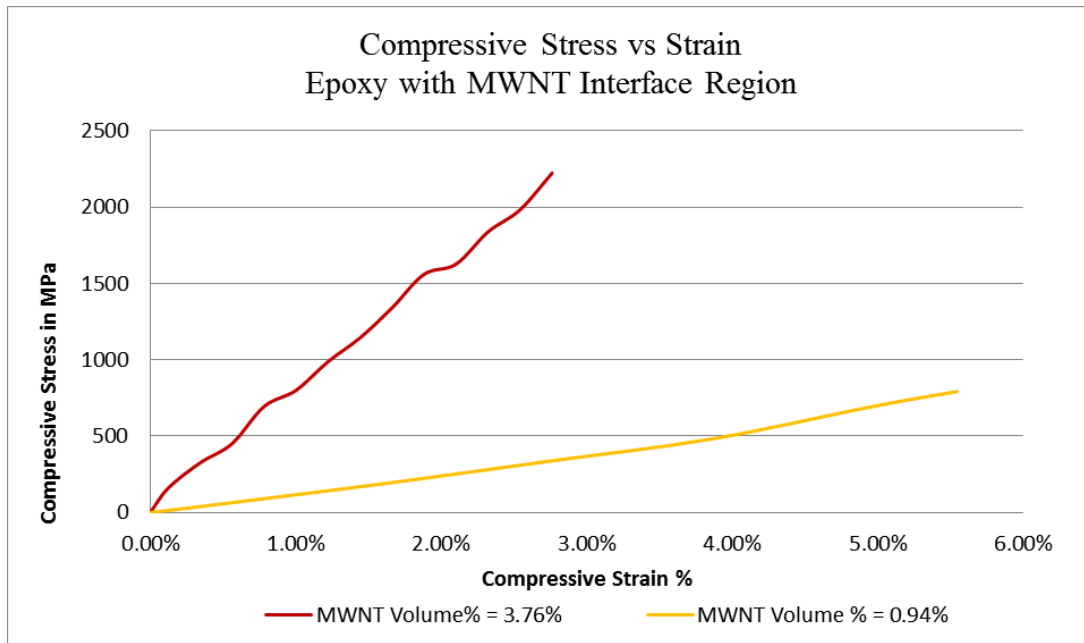


Figure 4.10: Compressive Stress Vs Strain for Epoxy with One and Four MWNTs at a Strain Rate Of 1×10^{10} /sec at 300 K

TABLE 4.8: Modulus of the Interface Region between Epoxy-MWNT from MD Simulations And Multiscale Approach Computed at a Strain Rate Of 0.001 /sec

% Volume Fraction of MWNT in epoxy	Modulus (GPa)
0.94%	13
3.76%	30

Interpolating these data in Table 4.8 to 16.1 GPa measured in the nanoindentation test, the estimated volume fraction of MWNT at the fiber-matrix interphase in the nanoindentation tests was predicted as 1.45%.

(b) Three-point Bending Test of Unidirectional IM7/MWNT/Epoxy Composite Beam

The next step was to calculate the relationship between the volume fraction of MWNT and the modulus of the IM7/MWNT/Epoxy composite fiber. For this, a micromechanical approach was derived. The first step was to find the relationship between the volume fraction of MWNT wrapped over carbon fiber with the bias angle effect. Figure 4.11 describes the interface region between carbon fiber of radius R_i with wrapped MWNT (with epoxy) at a bias angle α along the carbon fiber longitudinal direction X_1 .

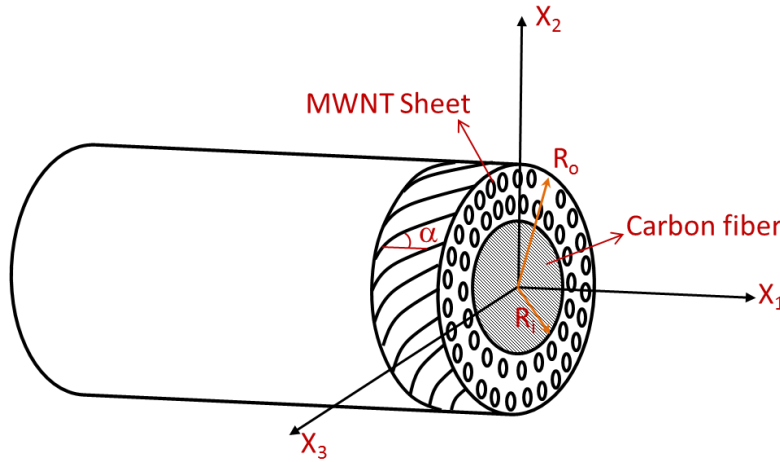


Figure 4.11: Schematic of MWNT Sheet Scrolled Single Carbon Fiber RVE

Let R_i be the inner radius of MWNT sheet and R_o the outer radius.

From micromechanics, assuming iso-strain applied in X_1 direction to the RVE in figure 4.11, the total force is X_1 is:

$$F_1 = E_{MWNT} \pi (R_o^2 - R_i^2) \epsilon_1 + E_F \pi R_i^2 \epsilon_1 \quad (4.4)$$

where $E_{MWNT}(\alpha)$ is the elastic modulus of MWNT sheet in X_1 – Direction, E_F is the Elastic modulus of carbon fiber. But, the total force on the MWNT-carbon fiber interface in the X_1 direction is also given by

$$F_1 = E_{MWNT-CF} \pi R_o^2 \epsilon_1 \quad (4.5)$$

Equating equations (4.4) and (4.5)

$$\begin{aligned} E_{MWNT-CF} &= E_{MWNT}(\alpha) \left(1 - \frac{R_i^2}{R_o^2} \right) + E_F \frac{R_i^2}{R_o^2} \\ E_{MWNT-CF} &= E_{MWNT}(\alpha) V_{MWNT} + E_F V_F \end{aligned} \quad (4.6)$$

where, V_{MWNT} is the volume fraction of MWNT and V_F is the volume fraction of carbon fiber.

The effect of wrapping angle α (bias angle) on the modulus of the wrapped MWNT ($E_{MWNT}(\alpha)$) can be described by equation 4.7 [9]

$$\frac{1}{E_{MWNT}(\alpha)} = \frac{1}{E_{1MWNT}} \cos^4 \alpha + \left[\frac{1}{G_{12MWNT}} - \frac{2\nu_{12}}{E_{1MWNT}} \right] (\sin^2 \alpha)(\cos^2 \alpha) + \frac{1}{E_{2MWNT}} \sin^4 \alpha \quad (4.7)$$

At the lamina level, for the whole composite, that is, MWNT wrapped over carbon fiber embedded in epoxy matrix, the modulus of the composite was calculated using equation (4.8) (rule of mixtures) , where $V_{MWNT-CF}$ is 1.45% as calculated from the multiscale approach and the nanoindentation results.

$$E_{1_{comp}}(\alpha) = E_{MWNT-CF}(\alpha) V_{MWNT-CF} + E_M V_M \quad (4.8)$$

Eqn (4.8) provides the longitudinal modulus of the composite laminate and includes the volume fraction of added MWNT at a given bias angle. It was used to compare multiscale model predictions for a three point bending test for a laminate conducted at UT-Dallas, and a

relationship between the slope of the load versus deflection of the composite beam was derived as follows:

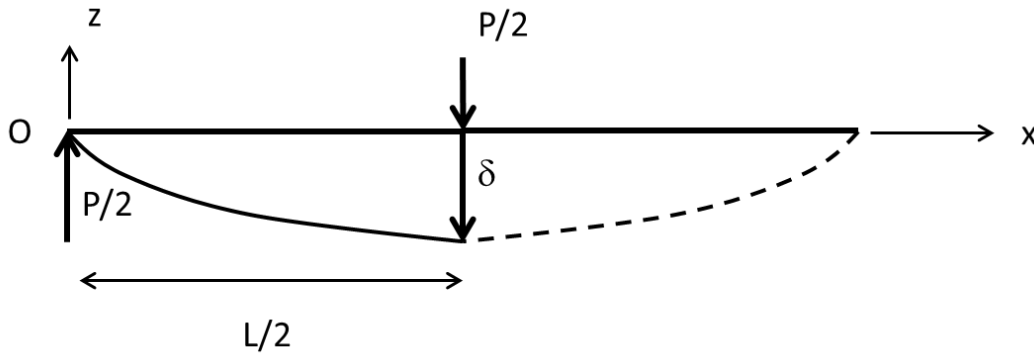


Figure 4.12: 3-Point Bending Schematic

$$M_x = D_{11}K_x = D_{11} \frac{\partial^2 w}{\partial x^2}$$

But $M_x = \frac{Px}{2}$ (Clockwise + $0 \leq X \leq L/2$)

Therefore,
$$D_{11} \frac{d^2 y}{dx^2} = \frac{P}{2} x$$

$$\frac{dw}{dx} = \frac{P}{2D_{11}} \frac{x^2}{2} + c_1$$

Since, $\left. \frac{dw}{dx} \right|_{x=\frac{L}{2}} = 0$ (from symmetry)

$$c_1 = -\frac{PL^2}{16D_{11}}$$

Integrating again,

$$w(x) = -\frac{PL^2x}{16D_{11}} + \frac{Px^3}{12D_{11}} + c_2$$

At $x = 0$, $w(0) = 0$, giving $c_2 = 0$

Therefore, $w(x) = \frac{P}{48D_{11}}[4x^3 - 3L^2x]$

At $x = L/2$, $w(x) = \delta = \frac{P}{48D_{11}} \left[\frac{4L^3}{8} - \frac{3L^3}{2} \right] = \frac{-PL^3}{48D_{11}}$ (4.9)

But, $D_{11} = \frac{1}{12} \bar{Q}_{11} h_{LAM}^3 b_{LAM} = \frac{1}{12} b_L h_L^3 \left(\frac{E_{1comp}(\alpha)}{1 - \nu_{12}\nu_{21}} \right)$ (4.10)

Substitute equation (7) in (6),

$$\delta = \frac{-PL^3}{48D_{11}} = \frac{-PL^3}{4b_L h_L^3} \left(\frac{1 - \nu_{12}\nu_{21}}{E_{1comp}(\alpha)} \right)$$
 (4.11)

Defining the slope of P - δ as m ,

$$m = \frac{P}{\delta} = \frac{4b_L h_L^3 E_1(\alpha)}{L^3 (1 - \nu_{12} \nu_{21})} \quad (4.12)$$

$$E_{1_{comp}}(\alpha) = \frac{m L^3 (1 - \nu_{12} \nu_{21})}{4b_L h_L^3}$$

This relationship between the slope and the modulus of the composite can directly be related to the added volume fraction of MWNT and its bias angle. For a specimen dimensions with a thickness (h_L) of 0.54 mm, width (b_L) of 4.82 mm and length (L) of 17.28 mm (ASTM D7264), the slope of the three-point bend specimen is predicted to be $m = 2.00$. This does not agree well with the experimentally measured slope of 8.42. The reason for this discrepancy is likely due to the use of the Oliver-Pharr equation for interpretation of the nanoindentation data as the Oliver-Pharr equation has been shown to be inaccurate for anisotropic materials.

CHAPTER 5

CONCLUSIONS AND FUTURE WORK

5.1 Conclusions:

This dissertation develops a unique multiscale approach to predict the enhancement in the compressive strength of unidirectional CFRP composites at room temperature (300 K) when MWNTs are introduced in the interface region between the carbon fiber and the epoxy. Nanoscale analyses were performed, using Molecular Dynamics tool, to study the interface region between the epoxy and MWNTs. A hierarchical multiscale approach was developed to use the nanoscale data MD as input to the microscale rule of mixtures, which finally feeds into the macroscale modified Argon's formula to compute the compressive strength of the carbon composite, with and without MWNT. This methodology was verified by performing the same RVE based analysis on baseline epoxy model and comparing the calculated compressive strength with literature data for epoxy. A study on the influence of overwrap angle of MWNTs on the Carbon fiber was also performed, and three different cases of overwrap, namely, 0° , 45° and 90° were studied and compared. ReaxFF potential was used to define the force field potentials of the molecular model of the epoxy and MWNTs, because of its inherent ability to create and break bonds between atoms.

The compressive strength calculated for the baseline epoxy case with 50% volume fraction of carbon fiber at room temperature (300 K) was calculated to be 665 MPa, which is in good agreement with the experimentally observed range of 550-800 MPa. A novel power-law methodology was employed to map the high MD strain rates down to lower strain rates typically used in quasi-static materials characterization experiments. One and four MWNTs (0.94 vol%

and 3.76 vol% of MWNTs) were introduced in the epoxy RVE, and an improvement of 19% and 34.3% respectively was observed over baseline case, respectively. To study the influence of overwrap angle of MWNTs on the carbon fiber, a different approach was used, where the angle of the shear deformation was switched on the RVE of epoxy/MWNT interface region. Three cases of MWNT overwrap angles were compared for 0.94 vol% case, namely, 0° , 45° and 90° . With four MWNTs embedded in the epoxy (3.76 vol % case), two overwrap angles were compared, 0° and 90° . It was observed that, with four MWNTs wrapped around carbon fiber at 90° bias angle, the compressive strength calculated was 20% higher than the case with MWNT wrapped at 0° bias angle around the carbon fiber. This was verified with Halpin-Tsai calculations. From both the MD simulation results and the Halpin-Tsai calculations, an improvement in the shear modulus was observed for 90° bias angle case over the 0° bias angle case, for the matrix with four MWNTs embedded in the epoxy. However, the Halpin-Tsai analytical model predicts a much larger (23%) improvement in the shear modulus of the matrix with MWNT at 90° bias angle, whereas the MD model predicts only an increase of 3%. The discrepancy is likely due to the fact that Halpin-Tsai model is a two-dimensional micromechanical model which does not account for the non-bonded interactions between the MWNT and the epoxy matrix. Hence, maximum enhancement in the compressive strength of the CFRP is predicted on overwrapping carbon fiber with MWNTs at 90° bias angle. Table 5.1 summarizes all the shear modulus of the matrix, composite and the compressive strength of the composite for all the case studies discussed in this dissertation. Finally, the multiscale model from the MD results was compared with experimental data from nanoindentation tests and three-point bending tests on MWNT wrapped carbon-fiber/epoxy composite beams performed at UT-Dallas.

Table 5.1: Compressive Strength Comparison for Cases I-VI, at the Reference Strain Rate Of 0.01 /sec

	<u>Shear Modulus of the Matrix (G_m)</u>	<u>Shear Modulus of the Composite (G_{12c})</u>	<u>Compressive Strength of the Composite (σ_c)</u>
Baseline CFRP (Case I)	7581 MPa	6026 MPa	665 MPa
CFRP wrapped with 3.76 vol% MWNTs at 90° bias angle (Case II)	7875 MPa	6116 MPa	893 MPa
CFRP wrapped with 3.76 vol% MWNTs at 0° bias angle (Case III)	7701 MPa	6063 MPa	763 MPa
CFRP wrapped with 0.94 vol% MWNT at 90° bias angle (Case IV)	7708 MPa	6066 MPa	791 MPa
CFRP wrapped with 0.94 vol% MWNT at 0° bias angle (Case V)	7684 MPa	6058 MPa	697 MPa
CFRP wrapped with 0.94 vol% MWNT at 45° bias angle (Case VI)	7720 MPa	6069 MPa	722 MPa

5.2 Future Work

Suggested future works on this methodology are as follows:

- Modeling and analyzing four MWNTs embedded in the epoxy system at 45° bias angle (i.e., 3.76 vol%) to the carbon fiber.
- Running more shear deformation MD simulations at lower strain rates.
- Changing the chirality and hence the diameter of the MWNTs and changing the number of carbon nanotubes from DWNTs to SWNTs or more to run a parametric study on the effect of the diameter and the number of tubes embedded in the epoxy.
- Model the RVE of MWNT embedded in epoxy including the presence of voids and defects.
- The enhancement in the electrical and thermal properties of the CFRP on being overwrapped with CNT sheets can also be studied through MD analysis.
- Data from nanoscale MD simulations can be incorporated in the other microscale techniques like generalized method of cells (GMC) and further can be used in the macroscale finite element analysis.
- A better parameterization of reactive force field can lead to more accurate predictions.
- Using CNT diameters of about 10 nm, which match the actual diameters fabricated and used in the industries.

REFERENCES

1. Archive, B.I. A Quarterly Publication, Quarter 4, Issue 24. Aero Magazine 2006 06.28.2017]; Available From: http://www.Boeing.com/Commercial/Aeromagazine/Articles/Qtr_4_06/Article_04_2.html.
2. Xwb, A. Innovation. 2016 06.28.2017]; Available From: <http://www.A350xwb.com/Innovation/>.
3. Zhou, Y., Et Al., Improvement In Electrical, Thermal And Mechanical Properties Of Epoxy By Filling Carbon Nanotube. Express Polymer Letters, 2008. 2(1): P. 40-48.
4. Kumar, A., Et Al., Fracture Properties Of Nanographene Reinforced Epon 862 Thermoset Polymer System. Composites Science And Technology, 2015. 114: P. 87-93.
5. Gojny, F., Et Al., Carbon Nanotube-Reinforced Epoxy-Composites: Enhanced Stiffness And Fracture Toughness At Low Nanotube Content. Composites Science And Technology, 2004. 64(15): P. 2363-2371.
6. Liu, W., S.V. Hoa, And M. Pugh, Fracture Toughness And Water Uptake Of High-Performance Epoxy/Nanoclay Nanocomposites. Composites Science And Technology, 2005. 65(15): P. 2364-2373.
7. Wicks, S.S. And B.L. Wardle, Interlaminar Fracture Toughness Of Laminated Woven Composites Reinforced With Aligned Nanoscale Fibers: Mechanisms At The Macro, Micro, And Nano Scales, In 54th Aiaa/Asme/Asce/Ahs/Asc Structures, Structural Dynamics, And Materials Conference. 2013, American Institute Of Aeronautics And Astronautics.
8. Rafiee, M.A., Et Al., Fracture And Fatigue In Graphene Nanocomposites. Small, 2010. 6(2): P. 179-183.
9. Jones, R.M., Mechanics Of Composite Material. Second Ed.: Taylor And Francis.
10. Rosen, B.W., Mechanisms Of Composite Strengthening, In Fiber Composite Materials. 1965, American Society Of Metals. P. 37-75.
11. Swadener, J.G., K.M. Liechti, And A.L.D. Lozanne, The Intrinsic Toughness And Adhesion Mechanisms Of A Glass/Epoxy Interface. Journal Of The Mechanics And Physics Of Solids, 1999. 47(2): P. 223-258.
12. Ding, W., Et Al., Direct Observation Of Polymer Sheathing In Carbon Nanotube–Polycarbonate Composites. Nano Letters, 2003. 3(11): P. 1593-1597.
13. Hussain, F., Et Al., Review Article: Polymer-Matrix Nanocomposites, Processing, Manufacturing, And Application: An Overview. Journal Of Composite Materials, 2006. 40(17): P. 1511-1575.

14. Thostenson, E.T., C. Li, And T.-W. Chou, Nanocomposites In Context. *Composites Science And Technology*, 2005. 65(3): P. 491-516.
15. Dalton, A.B., Et Al., Super-Tough Carbon-Nanotube Fibres. *Nature*, 2003. 423(6941): P. 703-703.
16. Jia, J., Et Al., A Comparison Of The Mechanical Properties Of Fibers Spun From Different Carbon Nanotubes. *Carbon*, 2011. 49(4): P. 1333-1339.
17. Frankland, S.J.V. And V.M. Harik, Analysis Of Carbon Nanotube Pull-Out From A Polymer Matrix. *Surface Science*, 2003. 525(1): P. L103-L108.
18. Chowdhury, S.C. And T. Okabe, Computer Simulation Of Carbon Nanotube Pull-Out From Polymer By The Molecular Dynamics Method. *Composites Part A: Applied Science And Manufacturing*, 2007. 38(3): P. 747-754.
19. Sager, R.J., Et Al., Effect Of Carbon Nanotubes On The Interfacial Shear Strength Of T650 Carbon Fiber In An Epoxy Matrix. *Composites Science And Technology*, 2009. 69(7): P. 898-904.
20. Fang, C., Et Al., Enhanced Carbon Nanotube Fibers By Polyimide. *Applied Physics Letters*, 2010. 97(18): P. 181906.
21. Grimmer, C.S. And C.K.H. Dharan, Enhancement Of Delamination Fatigue Resistance In Carbon Nanotube Reinforced Glass Fiber/Polymer Composites. *Composites Science And Technology*, 2010. 70(6): P. 901-908.
22. Mei, L., Et Al., Grafting Carbon Nanotubes Onto Carbon Fiber By Use Of Dendrimers. *Materials Letters*, 2010. 64(22): P. 2505-2508.
23. Zhang, F.-H., Et Al., Interfacial Shearing Strength And Reinforcing Mechanisms Of An Epoxy Composite Reinforced Using A Carbon Nanotube/Carbon Fiber Hybrid. *Journal Of Materials Science*, 2009. 44(13): P. 3574-3577.
24. Godara, A., Et Al., Interfacial Shear Strength Of A Glass Fiber/Epoxy Bonding In Composites Modified With Carbon Nanotubes. *Composites Science And Technology*, 2010. 70(9): P. 1346-1352.
25. Siddiqui, N.A., Et Al., Tensile Strength Of Glass Fibres With Carbon Nanotube-Epoxy Nanocomposite Coating. *Composites Part A: Applied Science And Manufacturing*, 2009. 40(10): P. 1606-1614.
26. Zhang, Y.C. And X. Wang, Thermal Effects On Interfacial Stress Transfer Characteristics Of Carbon Nanotubes/Polymer Composites. *International Journal Of Solids And Structures*, 2005. 42(20): P. 5399-5412.

27. Qian, H., Et Al., Carbon Nanotube Grafted Carbon Fibres: A Study Of Wetting And Fibre Fragmentation. *Composites Part A: Applied Science And Manufacturing*, 2010. 41(9): P. 1107-1114.
28. Fleck, N.A. And B. Budiansky, Compressive Failure Of Fibre Composites Due To Microbuckling, In *Inelastic Deformation Of Composite Materials: Iutam Symposium*, Troy, New York, May 29 – June 1, 1990, G.J. Dvorak, Editor. 1991, Springer New York: New York, Ny. P. 235-273.
29. Kumar, I.P., P.M. Mohite, And S. Kamle, Axial Compressive Strength Testing Of Single Carbon Fibres. *Archives Of Mechanics*, 2013. 65(1): P. 27-43.
30. Potter, W.G., *Epoxide Resins*. 1970, London,,: Iliffe. 7 , 248 P.
31. Kobayashi, M., F. Sanda, And T. Endo, Application Of Phosphonium Ylides To Latent Catalysts For Polyaddition Of Bisphenol A Diglycidyl Ether With Bisphenol A: Model System Of Epoxy-Novolac Resin. *Macromolecules*, 1999. 32(15): P. 4751-4756.
32. Nouri, N. And S. Ziaei-Rad, A Molecular Dynamics Investigation On Mechanical Properties Of Cross-Linked Polymer Networks. *Macromolecules*, 2011. 44(13): P. 5481-5489.
33. Tack, J.L. And D. Ford, Thermodynamic And Mechanical Properties Of Epon 862 With Curing Agent Detda By Molecular Simulation. 1 Online Resource.
34. Iijima, S., Helical Microtubules Of Graphitic Carbon. *Nature*, 1991. 354(6348): P. 56-58.
35. Ebbesen, T.W. And P.M. Ajayan, Large-Scale Synthesis Of Carbon Nanotubes. *Nature*, 1992. 358(6383): P. 220-222.
36. Thess, A., Et Al., Crystalline Ropes Of Metallic Carbon Nanotubes. *Science*, 1996. 273(5274): P. 483.
37. Oberlin, A., M. Endo, And T. Koyama, Filamentous Growth Of Carbon Through Benzene Decomposition. *Journal Of Crystal Growth*, 1976. 32(3): P. 335-349.
38. Thakre, P.R. And D.C. Lagoudas, Processing And Characterization Of Carbon Nanotubes Reinforced Epoxy Resin Based Multi-Scale Multi-Functional Composites. 1 Online Resource.
39. Yu, M.-F., Et Al., Tensile Loading Of Ropes Of Single Wall Carbon Nanotubes And Their Mechanical Properties. *Physical Review Letters*, 2000. 84(24): P. 5552-5555.
40. Thostenson, E.T., Et Al., Carbon Nanotube/Carbon Fiber Hybrid Multiscale Composites. *Journal Of Applied Physics*, 2002. 91(9): P. 6034-6037.

41. Tai, N.-H., M.-K. Yeh, And J.-H. Liu Enhancement Of The Mechanical Properties Of Carbon Nanotube/Phenolic Composites Using A Carbon Nanotube Network As The Reinforcement. Volume 42, Doi: 10.1016/J.Carbon.2004.06.002.
42. Biercuk, M.J., Et Al., Carbon Nanotube Composites For Thermal Management. Applied Physics Letters, 2002. 80(15): P. 2767-2769.
43. Choi, E.S., Et Al., Enhancement Of Thermal And Electrical Properties Of Carbon Nanotube Polymer Composites By Magnetic Field Processing. Journal Of Applied Physics, 2003. 94(9): P. 6034-6039.
44. Huang, Y. And R.J. Young, Interfacial Micromechanics In Thermoplastic And Thermosetting Matrix Carbon Fibre Composites. Composites Part A: Applied Science And Manufacturing, 1996. 27(10): P. 973-980.
45. He, H., Et Al., Mixed Resin And Carbon Fibres Surface Treatment For Preparation Of Carbon Fibres Composites With Good Interfacial Bonding Strength. Materials & Design, 2010. 31(10): P. 4631-4637.
46. Li, J., Interfacial Studies On The O₃ Modified Carbon Fiber-Reinforced Polyamide 6 Composites. Applied Surface Science, 2008. 255(5): P. 2822-2824.
47. Moon, C.K., Et Al., Effect Of Diameter And Surface Treatment Of Fiber On Interfacial Shear Strength In Glass Fiber/Epoxy And Hdpe. Journal Of Applied Polymer Science, 1992. 45(3): P. 443-450.
48. Qian, H., Et Al., Carbon Nanotube Grafted Silica Fibres: Characterising The Interface At The Single Fibre Level. Composites Science And Technology, 2010. 70(2): P. 393-399.
49. Zhang, Q., Et Al., Hierarchical Composites Of Carbon Nanotubes On Carbon Fiber: Influence Of Growth Condition On Fiber Tensile Properties. Composites Science And Technology, 2009. 69(5): P. 594-601.
50. Zeng, Y., Et Al., Design And Reinforcement: Vertically Aligned Carbon Nanotube-Based Sandwich Composites. Acs Nano, 2010. 4(11): P. 6798-6804.
51. Sharma, S.P. And S.C. Lakkad, Effect Of Cnts Growth On Carbon Fibers On The Tensile Strength Of Cnts Grown Carbon Fiber-Reinforced Polymer Matrix Composites. Composites Part A: Applied Science And Manufacturing, 2011. 42(1): P. 8-15.
52. Zhao, F. And Y. Huang, Improved Interfacial Properties Of Carbon Fiber/Epoxy Composites Through Grafting Polyhedral Oligomeric Silsesquioxane On Carbon Fiber Surface. Materials Letters, 2010. 64(24): P. 2742-2744.

53. Zhu, J., Et Al., Improving The Dispersion And Integration Of Single-Walled Carbon Nanotubes In Epoxy Composites Through Functionalization. *Nano Letters*, 2003. 3(8): P. 1107-1113.
54. Zhu, J., Et Al., Processing A Glass Fiber Reinforced Vinyl Ester Composite With Nanotube Enhancement Of Interlaminar Shear Strength. *Composites Science And Technology*, 2007. 67(7): P. 1509-1517.
55. Zhu, Y., C.E. Bakis, And J.H. Adair, Effects Of Carbon Nanofiller Functionalization And Distribution On Interlaminar Fracture Toughness Of Multi-Scale Reinforced Polymer Composites. *Carbon*, 2012. 50(3): P. 1316-1331.
56. Che, J., Et Al., Epoxy Composite Fibers Reinforced With Aligned Single-Walled Carbon Nanotubes Functionalized With Generation 0–2 Dendritic Poly(Amidoamine). *Chemistry Of Materials*, 2009. 21(8): P. 1471-1479.
57. Ma, W., Et Al., High-Strength Composite Fibers: Realizing True Potential Of Carbon Nanotubes In Polymer Matrix Through Continuous Reticulate Architecture And Molecular Level Couplings. *Nano Letters*, 2009. 9(8): P. 2855-2861.
58. Martinez-Rubi, Y., Et Al., Toughening Of Epoxy Matrices With Reduced Single-Walled Carbon Nanotubes. *Acs Applied Materials & Interfaces*, 2011. 3(7): P. 2309-2317.
59. Sui, X. And H.D. Wagner, Tough Nanocomposites: The Role Of Carbon Nanotube Type. *Nano Letters*, 2009. 9(4): P. 1423-1426.
60. Assael, M.J., Et Al., Measurements On The Enhancement Of The Thermal Conductivity Of An Epoxy Resin When Reinforced With Glass Fiber And Carbon Multiwalled Nanotubes. *Journal Of Chemical & Engineering Data*, 2009. 54(9): P. 2365-2370.
61. Kotaki, M., Et Al., Electrically Conductive Epoxy/Clay/Vapor Grown Carbon Fiber Hybrids. *Macromolecules*, 2006. 39(3): P. 908-911.
62. Zu, M., Et Al., The Effective Interfacial Shear Strength Of Carbon Nanotube Fibers In An Epoxy Matrix Characterized By A Microdroplet Test. *Carbon*, 2012. 50(3): P. 1271-1279.
63. Ganesan, Y., Et Al., Interface Toughness Of Carbon Nanotube Reinforced Epoxy Composites. *Acs Applied Materials & Interfaces*, 2011. 3(2): P. 129-134.
64. Özden-Yenigün, E., Y.Z. Menciloğlu, And M. Papila, Mwcnts/P(St-Co-Gma) Composite Nanofibers Of Engineered Interface Chemistry For Epoxy Matrix Nanocomposites. *Acs Applied Materials & Interfaces*, 2012. 4(2): P. 777-784.

65. Bekyarova, E., Et Al., Functionalized Single-Walled Carbon Nanotubes For Carbon Fiber–Epoxy Composites. *The Journal Of Physical Chemistry C*, 2007. 111(48): P. 17865-17871.
66. Cheng, Q., Et Al., Functionalized Carbon-Nanotube Sheet/Bismaleimide Nanocomposites: Mechanical And Electrical Performance Beyond Carbon-Fiber Composites. *Small*, 2010. 6(6): P. 763-767.
67. Tsotsis, T.K., Interlayer Toughening Of Composite Materials. *Polymer Composites*, 2009. 30(1): P. 70-86.
68. Fan, Z., M.H. Santare, And S.G. Advani, Interlaminar Shear Strength Of Glass Fiber Reinforced Epoxy Composites Enhanced With Multi-Walled Carbon Nanotubes. *Composites Part A: Applied Science And Manufacturing*, 2008. 39(3): P. 540-554.
69. Tseng, C.-H., C.-C. Wang, And C.-Y. Chen, Functionalizing Carbon Nanotubes By Plasma Modification For The Preparation Of Covalent-Integrated Epoxy Composites. *Chemistry Of Materials*, 2007. 19(2): P. 308-315.
70. Godara, A., Et Al., Influence Of Carbon Nanotube Reinforcement On The Processing And The Mechanical Behaviour Of Carbon Fiber/Epoxy Composites. *Carbon*, 2009. 47(12): P. 2914-2923.
71. Barber, A.H., Et Al., Fracture Transitions At A Carbon-Nanotube/Polymer Interface. *Advanced Materials*, 2006. 18(1): P. 83-87.
72. Barber, A.H., S.R. Cohen, And H.D. Wagner, Measurement Of Carbon Nanotube–Polymer Interfacial Strength. *Applied Physics Letters*, 2003. 82(23): P. 4140-4142.
73. Manoharan, M.P., Et Al., The Interfacial Strength Of Carbon Nanofiber Epoxy Composite Using Single Fiber Pullout Experiments. *Nanotechnology*, 2009. 20(29): P. 295701.
74. Desaegeer, M. And I. Verpoest, On The Use Of The Micro-Indentation Test Technique To Measure The Interfacial Shear Strength Of Fibre-Reinforced Polymer Composites. *Composites Science And Technology*, 1993. 48(1): P. 215-226.
75. Ureña, A., Et Al., Characterization Of Interfacial Mechanical Properties In Carbon Fiber/Aluminium Matrix Composites By The Nanoindentation Technique. *Composites Science And Technology*, 2005. 65(13): P. 2025-2038.
76. Tezcan, J., Et Al., Measurement And Analytical Validation Of Interfacial Bond Strength Of Pan-Fiber-Reinforced Carbon Matrix Composites. *Journal Of Materials Science*, 2008. 43(5): P. 1612-1618.
77. Haque, M.H., Thermal Oxidation Induced Degradation Of Carbon Fiber Reinforced Composites And Carbon Nanotube Sheet Enhanced Fiber/Matrix Interface For High

- Temperature Aerospace Structural Applications. 2012, The University Of Texas At Dallas: Ann Arbor. P. 177.
78. Zhang, M., Et Al., Strong, Transparent, Multifunctional, Carbon Nanotube Sheets. *Science*, 2005. 309(5738): P. 1215.
 79. Akepati, A.R., A Methodology For Predicting Fracture Toughness Of Nano-Graphene Reinforced Polymers Using Molecular Dynamics Simulations, In *Aerospace Engineering And Mechanics*. 2015, The University Of Alabama.
 80. Kumar, A., Multiscale Characterization And Modeling Of Progressive Failure In Nano-Graphene Reinforced Carbon/Epoxy Composites. 2016, The University Of Alabama.
 81. Leimkuhler, B.J., S. Reich, And R.D. Skeel, Integration Methods For Molecular Dynamics, In *Mathematical Approaches To Biomolecular Structure And Dynamics*, J.P. Mesirov, K. Schulten, And D.W. Sumners, Editors. 1996, Springer New York: New York, Ny. P. 161-185.
 82. Verlet, L., Computer "Experiments" On Classical Fluids. I. Thermodynamical Properties Of Lennard-Jones Molecules. *Physical Review*, 1967. 159(1): P. 98-103.
 83. Pastor, R.W., B.R. Brooks, And A. Szabo, An Analysis Of The Accuracy Of Langevin And Molecular Dynamics Algorithms. *Molecular Physics*, 1988. 65(6): P. 1409-1419.
 84. Hockney, R.W., Potential Calculation And Some Applications. 1970.
 85. Van Gunsteren, W.F. And H.J.C. Berendsen, A Leap-Frog Algorithm For Stochastic Dynamics. *Molecular Simulation*, 1988. 1(3): P. 173-185.
 86. Schofield, P., Computer Simulation Studies Of The Liquid State. *Computer Physics Communications*, 1973. 5(1): P. 17-23.
 87. Beeman, D., Some Multistep Methods For Use In Molecular Dynamics Calculations. *Journal Of Computational Physics*, 1976. 20(2): P. 130-139.
 88. Swope, W.C., Et Al., A Computer Simulation Method For The Calculation Of Equilibrium Constants For The Formation Of Physical Clusters Of Molecules: Application To Small Water Clusters. *The Journal Of Chemical Physics*, 1982. 76(1): P. 637-649.
 89. Buehler, M.J., *Atomistic Modeling Of Materials Failure*. 2008, New York ; London: Springer. Lxvii, 488 P.
 90. Berendsen, H.J.C., Et Al., Molecular Dynamics With Coupling To An External Bath. *The Journal Of Chemical Physics*, 1984. 81(8): P. 3684-3690.
 91. Andersen, H.C., Molecular Dynamics Simulations At Constant Pressure And/Or Temperature. *The Journal Of Chemical Physics*, 1980. 72(4): P. 2384-2393.

92. Nosé, S., A Unified Formulation Of The Constant Temperature Molecular Dynamics Methods. *The Journal Of Chemical Physics*, 1984. 81(1): P. 511-519.
93. Hoover, W.G. And B.L. Holian, Kinetic Moments Method For The Canonical Ensemble Distribution. *Physics Letters A*, 1996. 211(5): P. 253-257.
94. Alder, B.J. And T.E. Wainwright, Studies In Molecular Dynamics. I. General Method. *The Journal Of Chemical Physics*, 1959. 31(2): P. 459-466.
95. Fraser, L.M., Et Al., Finite-Size Effects And Coulomb Interactions In Quantum Monte Carlo Calculations For Homogeneous Systems With Periodic Boundary Conditions. *Physical Review B*, 1996. 53(4): P. 1814-1832.
96. Phillips, J.C., Et Al., Scalable Molecular Dynamics With Namd. *Journal Of Computational Chemistry*, 2005. 26(16): P. 1781-1802.
97. Le Roux, S. And V. Petkov, Isaacs - Interactive Structure Analysis Of Amorphous And Crystalline Systems. *Journal Of Applied Crystallography*, 2010. 43(1): P. 181-185.
98. Leech, J., J.F. Prins, And J. Hermans, Smd: Visual Steering Of Molecular Dynamics For Protein Design. *Ieee Computational Science And Engineering*, 1996. 3(4): P. 38-45.
99. Van Duin, A.C.T., Et Al., Reaxff: A Reactive Force Field For Hydrocarbons. *The Journal Of Physical Chemistry A*, 2001. 105(41): P. 9396-9409.
100. Jorgensen, W.L. And J. Tirado-Rives, The Opls [Optimized Potentials For Liquid Simulations] Potential Functions For Proteins, Energy Minimizations For Crystals Of Cyclic Peptides And Crambin. *Journal Of The American Chemical Society*, 1988. 110(6): P. 1657-1666.
101. Duffy, E.M. And W.L. Jorgensen, Prediction Of Properties From Simulations: Free Energies Of Solvation In Hexadecane, Octanol, And Water. *Journal Of The American Chemical Society*, 2000. 122(12): P. 2878-2888.
102. Weiner, S.J., Et Al., A New Force Field For Molecular Mechanical Simulation Of Nucleic Acids And Proteins. *Journal Of The American Chemical Society*, 1984. 106(3): P. 765-784.
103. Jorgensen, W.L., D.S. Maxwell, And J. Tirado-Rives, Development And Testing Of The Opls All-Atom Force Field On Conformational Energetics And Properties Of Organic Liquids. *Journal Of The American Chemical Society*, 1996. 118(45): P. 11225-11236.
104. Watkins, E.K. And W.L. Jorgensen, Perfluoroalkanes: Conformational Analysis And Liquid-State Properties From Ab Initio And Monte Carlo Calculations. *The Journal Of Physical Chemistry A*, 2001. 105(16): P. 4118-4125.

105. Plimpton, S., Fast Parallel Algorithms For Short-Range Molecular Dynamics. *Journal Of Computational Physics*, 1995. 117(1): P. 1-19.
106. Alexander, S. And A. Karsten, Extracting Dislocations And Non-Dislocation Crystal Defects From Atomistic Simulation Data. *Modelling And Simulation In Materials Science And Engineering*, 2010. 18(8): P. 085001.
107. Alexander, S., Visualization And Analysis Of Atomistic Simulation Data With Ovito—The Open Visualization Tool. *Modelling And Simulation In Materials Science And Engineering*, 2010. 18(1): P. 015012.
108. Argon, A.S., Fracture Of Composites. *Treatise On Materials Science & Technology*, 1972. 1: P. 79-114.
109. Budiansky, B., Micromechanics. *Computers & Structures*, 1983. 16(1): P. 3-12.
110. Creighton, C.J. And T.W. Clyne, The Compressive Strength Of Highly-Aligned Carbon-Fibre/Epoxy Composites Produced By Pultrusion. *Composites Science And Technology*, 2000. 60(4): P. 525-533.
111. Creighton, C.J., M.P.F. Sutcliffe, And T.W. Clyne, A Multiple Field Image Analysis Procedure For Characterisation Of Fibre Alignment In Composites. *Composites Part A: Applied Science And Manufacturing*, 2001. 32(2): P. 221-229.
112. Hussain, F., Et Al., E-Glass—Polypropylene Pultruded Nanocomposite: Manufacture, Characterization, Thermal And Mechanical Properties. *Journal Of Thermoplastic Composite Materials*, 2007. 20(4): P. 411-434.
113. Gilat, A., K. Goldberg Robert, And D. Roberts Gary, Strain Rate Sensitivity Of Epoxy Resin In Tensile And Shear Loading. *Journal Of Aerospace Engineering*, 2007. 20(2): P. 75-89.
114. Heyes, D.M., Pressure Tensor Of Partial-Charge And Point-Dipole Lattices With Bulk And Surface Geometries. *Physical Review B*, 1994. 49(2): P. 755-764.
115. Mechanical Properties Of Carbon Fibre Composite Materials, Fibre / Epoxy Resin (120°C Cure). July 2009 14 January 2016].
116. Afddl, J.C.H. And J.L. Kardos, The Halpin-Tsai Equations: A Review. *Polymer Engineering & Science*, 1976. 16(5): P. 344-352.
117. Chemicals, H.S. Product Bulletin Epikote[™] Resin/Epikure[™] Curing Agent W System. 2015; Available From: [Http://Www.Hexion.Com/Am/Epoxy-Resins-Curing-Agents-Modifiers/Technical-Data-Sheets/](http://Www.Hexion.Com/Am/Epoxy-Resins-Curing-Agents-Modifiers/Technical-Data-Sheets/).

118. Lu, J.P., Elastic Properties Of Carbon Nanotubes And Nanoropes. *Physical Review Letters*, 1997. 79(7): P. 1297-1300.
119. Oliver, W.C. And G.M. Pharr, An Improved Technique For Determining Hardness And Elastic Modulus Using Load And Displacement Sensing Indentation Experiments. *Journal Of Materials Research*, 2011. 7(6): P. 1564-1583.